Pacific Northwest
NATIONAL LABORATORY

PNNL-XXXXX

Preliminary Characterization and Evaluation on FFF Manufactured 316H and ODS Steels

September 2023

Carolyne A Burns
Saumyadeep Jana
Amrita Lall
Zachary C Kennedy
Michelle D Fenn
Joshua A Silverstein
Lorraine M Seymour
Isabella J Van Rooyen

U.S. DEPARTMENT OF ENERGY

Prepared for the U.S. Department of Energy
under Contract DE-AC05-76RL01830

DISCLAIMER

PACIFIC NORTHWEST NATIONAL LABORATORY
operated by
BATTELLE
for the
UNITED STATES DEPARTMENT OF ENERGY
under Contract DE-AC05-76RL01830

Printed in the United States of America

Available to DOE and DOE contractors from
the Office of Scientific and Technical Information,
P.O. Box 62, Oak Ridge, TN 37831-0062
www.osti.gov
ph: (865) 576-8401
fox: (865) 576-5728
email: reports@osti.gov

Available to the public from the National Technical Information Service
5301 Shawnee Rd., Alexandria, VA 22312
ph: (800) 553-NTIS (6847)
or (703) 605-6000
email: info@ntis.gov
Online ordering: http://www.ntis.gov

Preliminary Characterization and Evaluation on FFF Manufactured 316H and ODS Steels

September 2023

Carolyne A Burns
Saumyadeep Jana
Amrita Lall
Zachary C Kennedy
Michelle D Fenn
Joshua A Silverstein
Lorraine M Seymour
Isabella J Van Rooyen

Prepared for
the U.S. Department of Energy
under Contract DE-AC05-76RL01830

Pacific Northwest National Laboratory
Richland, Washington 99354

Summary

The Advanced Materials and Manufacturing Technology (AMMT) program develops cross-cutting technologies in support of a broad range of nuclear reactor technologies and maintains U.S. leadership in materials and manufacturing technologies for nuclear energy applications. The overarching vision of AMMT is to accelerate the development, qualification, demonstration, and deployment of advanced materials and manufacturing technologies to enable reliable and economical nuclear energy.

Solid-state advanced manufacturing techniques can overcome some of the challenges in liquid-based additive manufacturing (AM) processes and should therefore be considered in material design and manufacturing as well. The work presented in this report forms part of a study on solid-state AM techniques of 316 stainless steels (SS) and oxide dispersion strengthened (ODS) steel components and supports the vision and goals of the AMMT program relevant to accelerate the development and deployment of advanced manufacturing processes. Achieving this can provide a safety improvement through larger safety margins, economic benefit for higher efficiency during operation, and a cost reduction through more effective manufacturing processes and less waste.

This study provides preliminary information on development of the fused-filament fabrication (FFF) process using different powder types to demonstrate the sensitivity, and therefore the characterization of these sample components. The full solid-state manufacturing feasibility study will be completed and reported in a final feasibility evaluation during 2025. The study investigation used two 14YWT ODS powder batches, which provided information and the effect of different powder morphologies on manufacturability. The two 316SS powders demonstrated the effect of powder size on the manufacturability using FFF. Two product forms, namely a honeycomb structure and flat samples, were manufactured to demonstrate the flexibility of product form.

Both ODS steel and 316H custom filaments were successfully fabricated with a powder loading of 65% and 62%, respectively. Specific filament fabrication and printing parameters for each material type and powder were determined to achieve the successful printing, and therefore show feasibility to use FFF for component manufacturing and capability at Pacific Northwest National Laboratory (PNNL). However, process optimization for fully dense parts is necessary and the scalability needs further work.

The research results in this report provide evidence that it is feasible to print ODS steel as well as 316H SS using the solid-state FFF process with the following conclusions:

- The filament fabrication process and printing are sensitive for the powder morphology, size, and size distribution mainly due to the flowability of filament extrusion as well as sinter effectiveness.
- Custom powder can be used for FFF, so an in-house PNNL capability was developed enabling ODS and 316H SS powder loading techniques.
- Although effective printing and subsequent sintering did occur, further optimization is needed to fully fabricate structural sound components.

Acknowledgments

The research presented here was supported by the Advanced Materials and Manufacturing Technology Program of the Department of Energy's (DOE's) Office of Nuclear Energy. PNNL is a multiprogram national laboratory operated for DOE by Battelle Memorial Institute under Contract No. DE-AC05-76RL01830. PNNL would like to thank Dr Xuan Zhang (Argonne National Laboratory) for providing us with the 316H stainless steel powder used in this study. We would like to acknowledge Dr. Stuart Maloy, Dr. David Hoelzer, and Prof. G. Robert Odette for providing the 14YWT powder (called Batch 1) for this study. The production of the 14YWT powder was funded by the DOE Global Nuclear Energy Partnership program in 2008 subcontract-70553-001-09. Dr T.S. Byun from Oak Ridge National Laboratory is thanked for sharing of the smaller than 325 mesh 14YWT (called Batch 2) material. Chinthaka Silva is thanked for his review of the SEM interpretation.

Acronyms and Abbreviations

3D	three-dimensional
AM	additive manufacturing
AMMT	Advanced Materials and Manufacturing Technology
ANL	Argonne National Laboratory
BSE	backscattered electron
EBSD	electron backscatter diffraction
EDS	electron dispersive X-ray spectroscopy
FFF	fused-filament fabrication
ICP-MS	inductively coupled plasma mass spectrometry
ODS	oxide dispersion strengthened
PNNL	Pacific Northwest National Laboratory
PSD	particle size distribution
SEI	secondary electron imaging
SEM	scanning electron microscope
SS	stainless steel

Contents

Figures

Tables

1.0 Introduction

The Advanced Materials and Manufacturing Technology (AMMT) program develops cross-cutting technologies in support of a broad range of nuclear reactor technologies and maintains U.S. leadership in materials and manufacturing technologies for nuclear energy applications. The overarching vision of the AMMT program is to accelerate the development, qualification, demonstration, and deployment of advanced materials and manufacturing technologies to enable reliable and economical nuclear energy [1]

The AMMT program will exploit additive manufacturing (AM) to develop and optimize reactor materials and introduce new high-performance materials into nuclear energy systems. AM is an innovative technique to produce components at near-net shape with minimal machining. In some cases, the typical engineering alloys are not well suited to be produced through AM. Therefore, the AMMT program is further exploring other optimized alloy/manufacturing combinations for improved performance like increased radiation tolerance but also improved high-temperature strength, creep resistance, and environmental effects.

Solid-based AM techniques can overcome some of the challenges in liquid-based AM processes and should therefore be considered in material design and manufacturing as well. Solid-state AM techniques are generally divided into two broad categories, plastic deformation-based and sinter-based, depending on metallurgical bonding mechanisms, range of processible alloys, and resulting microstructures [2]. Binder jetting uses a binder to hold powder together, followed by sintering that consolidates the powder into a dense part without melting. This technology may be well suited for producing complex parts of oxide dispersion strengthened (ODS) alloys. Other advanced manufacturing techniques use severe deformation to impart high densities of dislocations in the material while forming it into a tube or plate form [3]. This does not allow one to produce complex shapes but can be used to produce tube, plate, or rod materials with a high density of sinks for extreme radiation tolerance.

The work presented in this report forms part of a study on solid-based AM techniques of 316 stainless steels (SS) and ODS steel components and supports the vision and goals of the AMMT program relevant to accelerate development and deployment of advanced manufacturing processes. Achieving this can provide a safety improvement through larger safety margins, economic benefit for higher efficiency during operation, and a cost reduction through more effective manufacturing processes and less waste.

1.1 Work Scope

The full work scope of Pacific Northwest National Laboratory’s (PNNL’s) solid-state manufacturing processes includes studies of developed 316SS and ODS steel sample components to demonstrate the feasibility of three solid-state manufacturing techniques: (i) fused-filament fabrication (FFF); (ii) shear-assisted processing and extrusion; and (iii) cold spray.

This report provides preliminary information on development of the FFF process using different powder types to demonstrate the sensitivity, and therefore the characterization of these sample components. This full solid-state manufacturing feasibility study will be completed and reported in a final feasibility evaluation during 2025.

The planned work scope for the FFF study is shown in Figure 1. Schematic of FFF feasibility study and process development phases., showing two 14YWT ODS powder batches which will provide information and the effect of different powder morphologies on the manufacturability with FFF. The two 316SS powders will demonstrate the effect of powder size on the manufacturability using FFF. Two product forms namely a honeycomb structure and flat samples were targeted to demonstrate the flexibility of product form while a solid billet would have been a stretched goal, pending on the success of the feasibility and development progress.

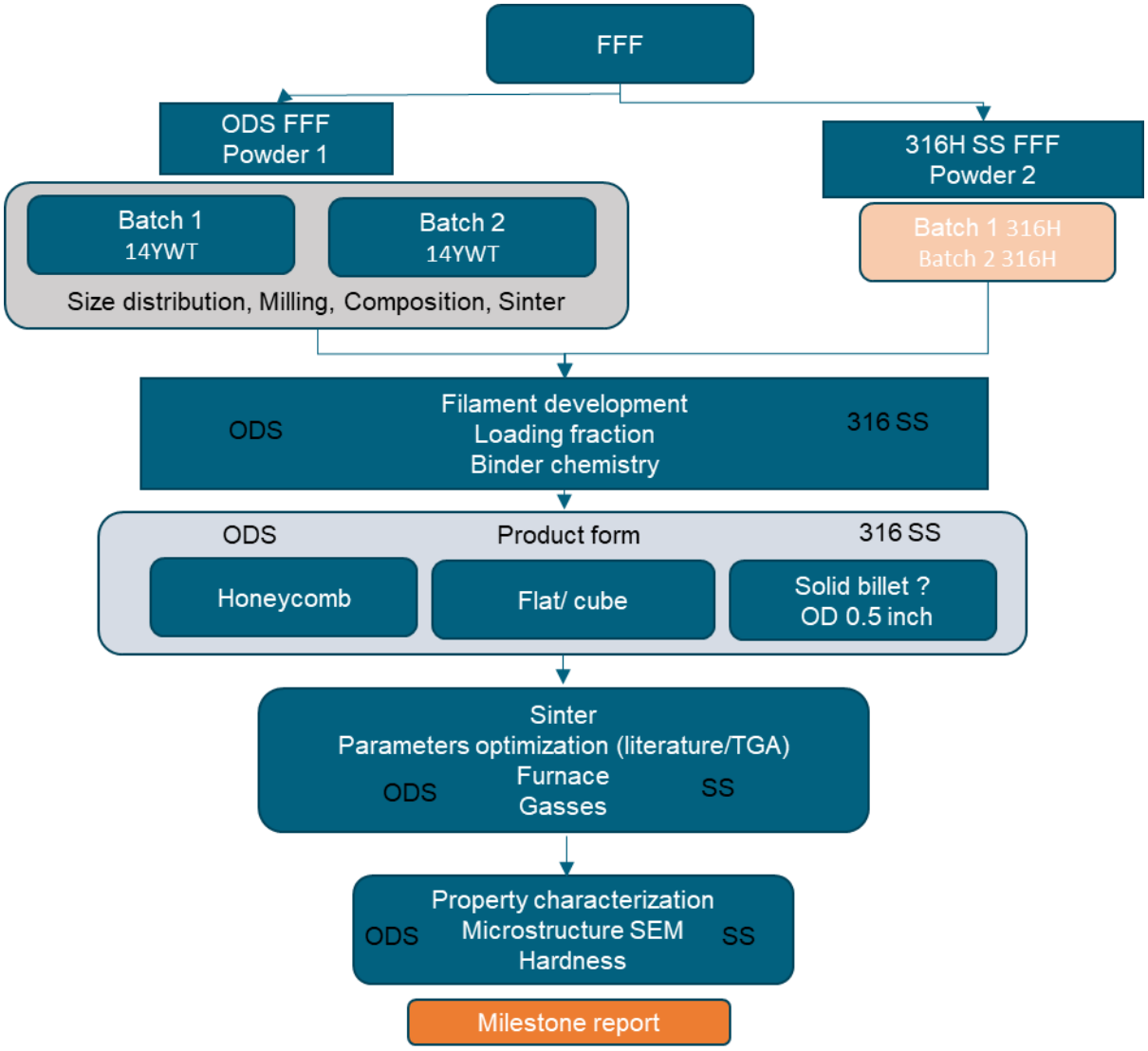

Figure 1. Schematic of FFF feasibility study and process development phases.

1.2 Objectives

The objectives of the full solid-state manufacturing feasibility are:

1. Assessment of benefits of solid-state advanced manufacturing processes for nuclear energy products. This will provide feasibility information on alternative routes for ODS steel manufacturing.

2. Demonstrate the sensitivity on final microstructural and residual stresses from the powder microstructure and composition.

More specifically, the work reported here will provide initial evaluation of the impact of powder morphology and sizes on the FFF process, and the feasibility and adaptability for different material systems, to use FFF for ODS steels and 316SS.

A preliminary sintering study was carried out to understand the sintering behavior 14YWT powder. This is critical since the particle size as received is larger than desired and densification through sintering is expected to be challenging. 14YWT was mixed with 7% by volume of PVB-79 and MEK and then allowed to mix overnight by rolling the container. Then the MEK was evaporated out by setting the mix on a hot plate at 90°C. The remaining mix was crushed using a mortar and pestle to remove any agglomeration during the drying process. Approximately 0.5 g of the crushed mix was pressed into cylindrical pellets of 6 mm diameter. The pellet was thermally debound and sintered using the temperature profile shown in Table 1 and Figure 2.

Table 1. Sintering profile used to sinter pressed 14YWT pellets.

Temperature	Hold Time (hrs)	Ramp Rate	Environment
300	4	1C/min	Ar
450	2	1C/min	Ar
1000	4	3C/min	Ar

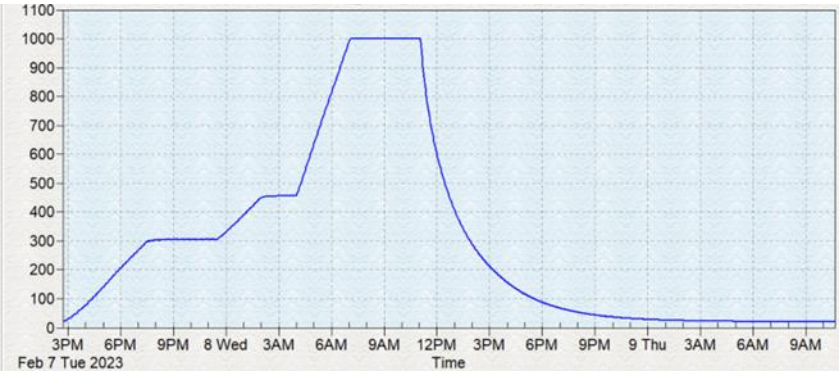

Figure 2. Temperature profile of the sintering trial of the pressed 14YWT.

The binder PVB-79 was removed gently by heating at a slow heating rate of 1°C/min and held at 300°C for 4 hours. Further isothermal hold of 2 hours was applied at 450°C to ensure complete removal of binder. The sample was then heated to 1000°C at a rate of 3°C/min and held for 4 hours. Although 1000°C is too low to ensure complete densification, it would show the tendency of the material toward neck formation and material transport. This current trial is useful to analyze how suitable the sieved 14YWT powder is for the solid-state AM process in its current state. Figure 3 shows a scanning electron microscope (SEM) image of the sintered pressed pellet. On pressing, the particles were positioned close to each other, but very little sintering or densification occurred. On closer observation a few necks were seen to have initiated. Figure 4 shows two examples of higher magnification SEM images showing neck formation between particles. This shows that there is scope for application of this manufacturing technique on this material if the feedstock powder can be improved to have a smaller size and lower aspect ratio. All the SEM images show abnormal grain growth and recrystallization. This can be attributed to the varying grain size and deformation during mechanical alloying.

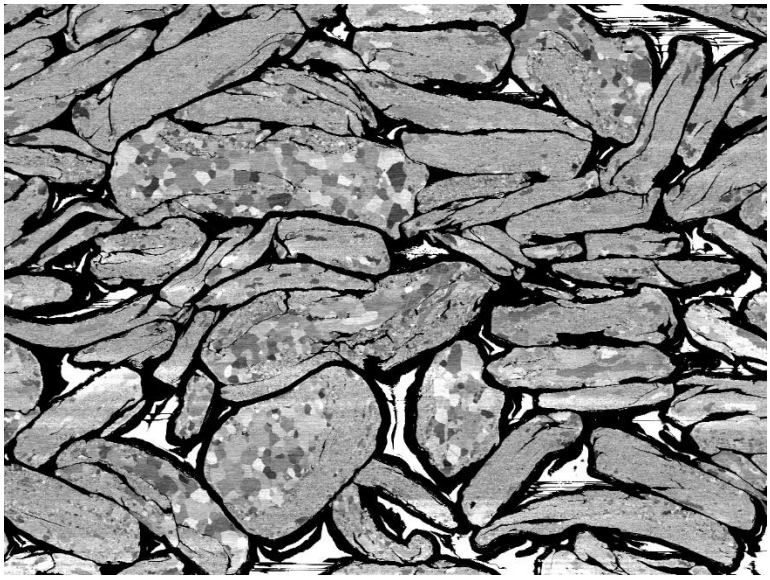

Figure 3. SEM image of the sintered pressed pellet.

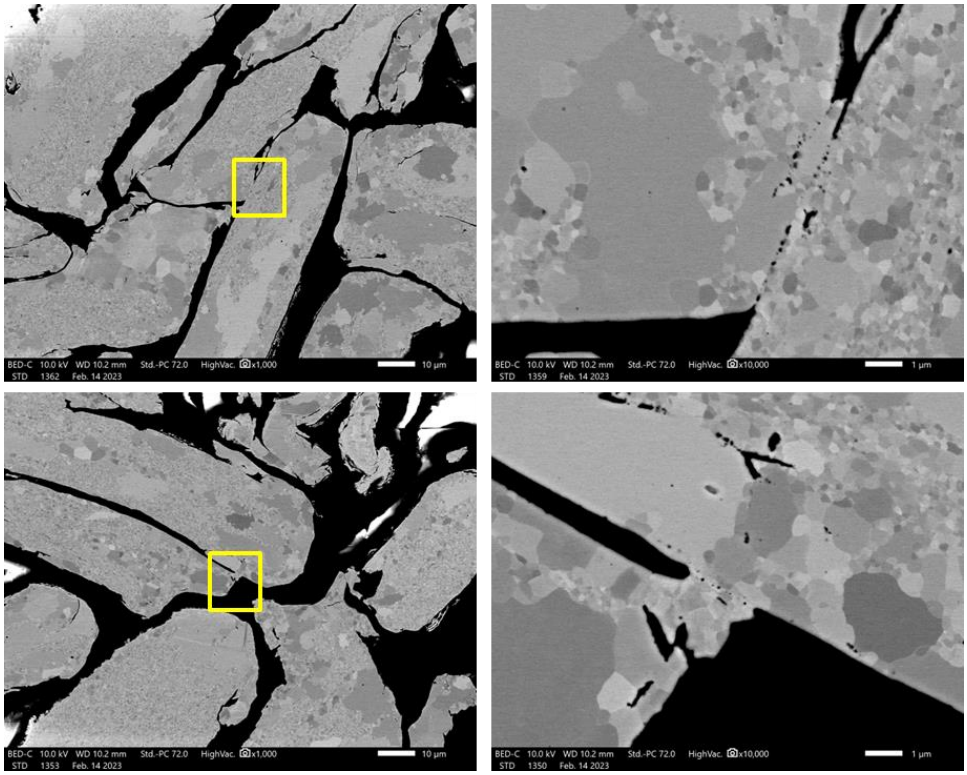

Figure 4. Higher magnification SEM image of sintered pressed pellet with necking initiation.

In contrast, finer spherical gas atomized FeCrAl samples that were pressed and sintered at the same temperature resulted in much better densification as can be seen in the SEM image from the etched sample, which had been pressed and sintered at 1000°C for 4 hours (Figure 5). This temperature is too low for complete densification of FeCrAl as well, but it is evident that diffusion and neck formation has started, and sintering has reached initial state.

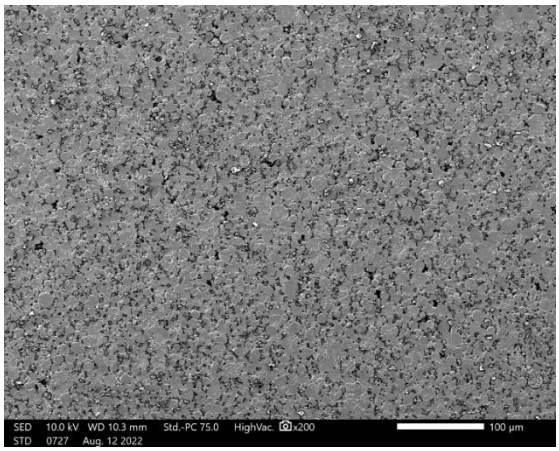

Figure 5. Etched sample, pressed and sintered at 1000°C for 4 hours.

1.3 Background on Solid-State Manufacturing Processes

With the increased use of AM, a near-net shape advanced manufacturing method that digitizes a component design into several layers, and subsequently a bulk shape is fabricated through layer-by-layer deposition, it provides tremendous opportunity to process steel powders into near-net shapes, with minimal waste of starting powder feedstock. In recent years, laser-based AM has been applied by several research groups to fabricate three-dimensional (3D) parts using mechanically alloyed ODS steel, 316L and 316H SS powders as the starting feedstock. [4, 5] Since laser-based AM involves melting and solidification of the steel powder repeatedly, it typically introduces a columnar grain structure, coarsening and slagging of strengthening oxide particles. Therefore, the mechanical performance and irradiation resistance of the 3D built remains inferior to comparable 3D parts obtained by hot working (e.g., hot isostatic press, hot extrusion) of steel powders [6].

From this aspect, solid-state AM offers an excellent alternative fabrication method for better microstructural control over matrix grain size and shape, size, shape, number density, and distribution of strengthening nanosized oxide particles. Specifically, we have investigated FFF, a solid-state sintering-based AM method, in fabricating 3D parts using mechanically alloyed ODS and 316H steel powders as starting feedstock. Since FFF uses high temperature sintering in the solid state to achieve final densification, the matrix grain remains equiaxed and there is better control on optimizing the size and distribution of nanosized oxide particles.

Figure 6 shows a schematic of the various steps associated with the FFF process, which includes, (i) filament fabrication, (ii) 3D shape printing, (iii) binder removal, and (iv) final high-temperature densification through sintering.

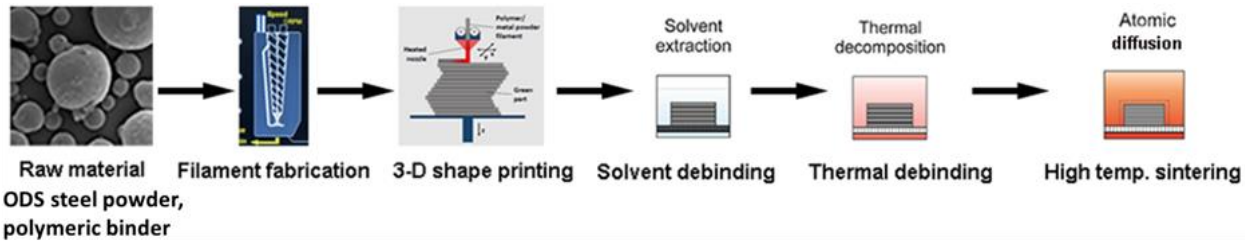

Figure 6. Schematic of FFF process.

2.0 Feasibility of FFF for Fabrication of ODS Steels

Two 14YWT ODS powder batches were used to provide information and the effect of different powder morphologies on manufacturability with FFF.

2.1 Experimentation on Powder 1 Batch 1

Mechanically alloyed 14YWT ODS steel powder was sourced and initially characterized. The powder is part of batch unique identifier 14YWT-V540-01-40H 3 and refers to the “Powder 1, Batch 1” in Figure 1.

2.1.1 Powder Characterization

2.1.1.1 Chemical composition

The chemical composition of the 14YWT powder was provided with the material and is captured in Table 2 as analysis A1, performed in November 2020. A sample of the material was sent to an outside vendor for chemical composition analysis via inductively coupled plasma mass spectrometry (ICP-MS) in January 2023. These data are also given as analysis A2. The two chemical compositions are comparable with the oxygen concentration remaining constant, indicating the alloy is resistant to oxidation at room temperature. Slight differences in concentration were observed for other elements analyzed, which could be attributed to a single data point and associated uncertainty of the method.

Table 2. Chemical composition of 14YWT.

ICP-MS	O	N	C	H	Fe	Cr	Y	W	Ti	Mn	Ni	Cu	Al	Si	Zr
A1-Wt%	0.097	nm	0.008	nm	nm	13.6	0.25	3.12	0.41	0.020	0.041	0.037	0.012	nm	nm
A2-wt%	0.119	0.007	0.011	0.002	81.59	14.4	0.21	3.12	0.40	0.019	0.016	0.004	0.022	0.062	<0.002

2.1.1.2 Powder Size Distribution

Powder size distribution was determined by two methods, (i) laser diffraction and (ii) SEM imaging. For particle size analysis using laser diffraction, 0.1 g of 14YWT was added to 30 ml of deionized water and three to five drops of TWEEN® 20 dispersant. The mix was sonicated 20 times to 9 watts by Microson ultrasonic cell disruptor to suspend the alloy powder in the deionized water/TWEEN 20 mixture. A Microtrac Sync M5000 was used to measure dynamic particle size and shape. The particle size distribution (PSD) plot is shown in Table 3.

Table 3. PSD of as-received 14YWT.

PSD by Vol%	Size, µm Laser Diffraction	Size, µm SEM ImageJ
d10	51.6	126.8
d50	102.5	190.3
d90	248	299

A bimodal distribution of powder size is noted, with the first peak being slightly below 100 µm and the second peak close to 200 µm. The as-received powder feedstock has a good mix of relatively fine and coarse particles. The as-received 14YWT powder was also analyzed using

SEM to gain insight of the particle morphology. The PSD analysis of the as-received 14YWT material (Figure 7) indicated that the powder is coarse, and that the packing density and other process parameter optimization may be challenging for densification through solid-state sintering, the final mechanism through which FFF-built parts attain high density.

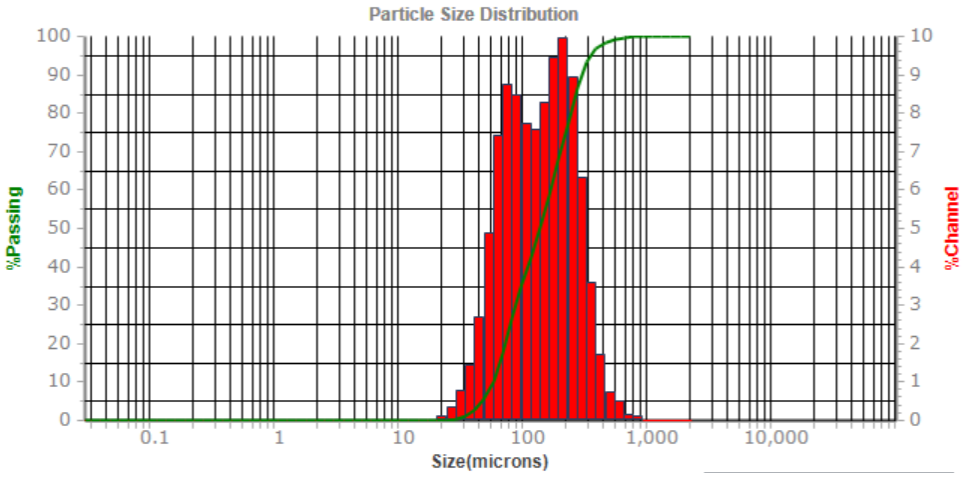

Figure 7. PSD of as-received 14YWT powder.

2.1.2 Powder Morphology: SEM Imaging

SEM imaging, shown in Figure 8, was performed using JEOL JSM-7600F secondary electrons with an accelerating voltage of 10 kV. The powder is highly magnetic and requires careful handling within the SEM. To help combat the highly magnetic nature of the particles, a larger working distance of 15 mm was chosen to avoid damage to the pole piece on the SEM.

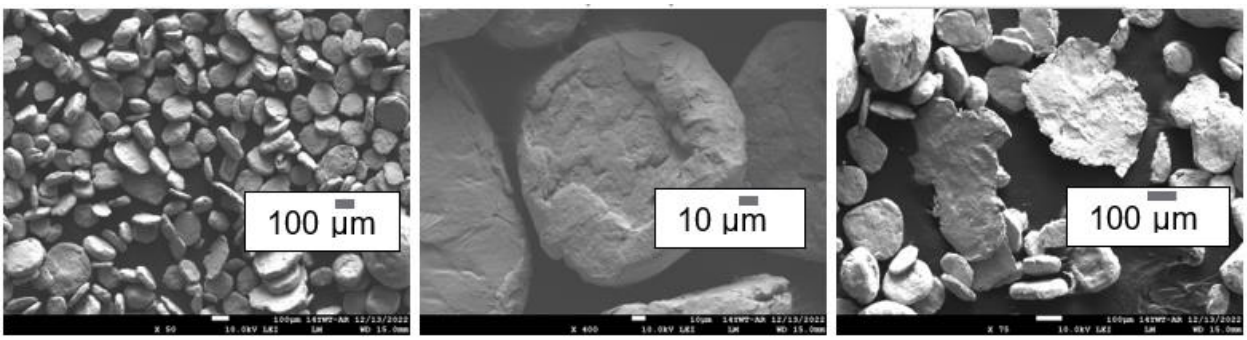

Figure 8. SEM images of as-received 14YWT powder.

As-received 14YWT powder has a flat, disc-like morphology typical of the mechanical milling process. There are some very large particles with diameters over 300 µm. SEM imaging confirms that the particle size is larger and does not have the high specific surface area (area/volume) needed for densification through sintering. ImageJ was used to perform image analysis to determine the PSD, select percentiles are presented in Table 3.

Based on the initial characterization of as-received 14YWT powder, the alloy was confirmed to have the reactive elements (Y and Ti) and dissolved oxygen needed for the formation of fine and thermally stable oxide particles (Y-Ti-O based) after heat treatment to provide strength at high temperature. However, the size and morphology of the powder is not ideal for solid-state

sintering-based densification methods. To resolve the problem, two routes of powder processing were used to create a finer feedstock of 14YWT powder.

- Additional mechanical milling to reduce particle size.
- Mechanical sieving to separate the inner fraction of 14YWT feedstock.

2.1.3 14YWT Powder Processing

2.1.3.1 Cryomilling Approach

A 700 g batch of as-received 14YWT powder was sent to California Nanotechnologies for cryomilling in liquid nitrogen. Use of the cryomilling method was expected to reduce particle size. Cryomilling was done in a high-energy attrition ball mill with the material submerged in liquid nitrogen and milled for 8 hours. Cryomilling produced a monodispersed PSD centered around 200 µm for 14YWT powder with a slight tail at 20 µm (Figure 9). The bimodal distribution of as-received powder has changed through both refinement and agglomeration. The initial cryomilling study did not refine the as-received 14YWT powder to the desired <20 µm particle size limit.

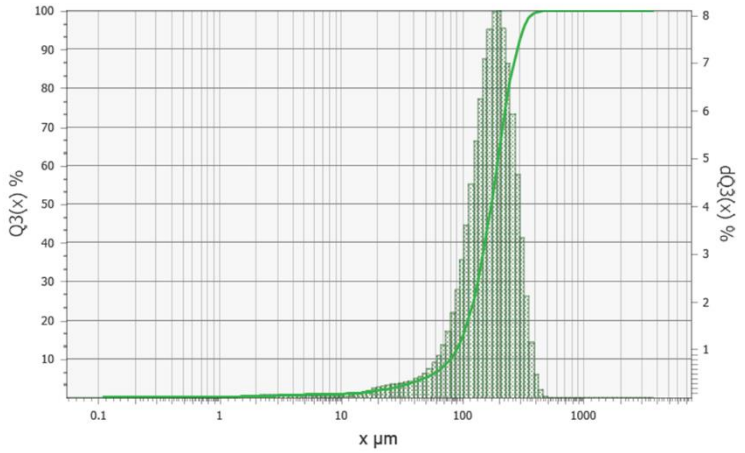

Figure 9. PSD of cryomilled 14YWT powder (data provided by California Nanotechnologies).

2.1.3.2 High-Energy Micromilling

Since particle size refinement could not be achieved through cryomilling, milling in a high-energy planetary mill was carried out at room temperature. The major difference between high-energy milling and the cryomilling approach is the relative size of powder feedstock that can be milled at a time. Cryomilling is capable of processing larger mass/volumes of material, with kg amounts of powder as the minimum amount of material processed at a time. Whereas high-energy milling can only process about ~50 g of powder feedstock for each trial. High-energy planetary milling was carried out using ZrO2 as the milling media, for different time durations (15-100 minutes). Figure 10 shows the PSD for 14YWT powder that was milled for 30, 60, and 100 minutes, respectively. The beneficial effect of high-energy planetary milling on refining particle size is immediately obvious. A larger volume fraction of particles <100 µm are generated with increased milling time from 30 to 100 minutes. Details of PSD measurement performed on high-energy micromilled powder is summarized in Table 4.

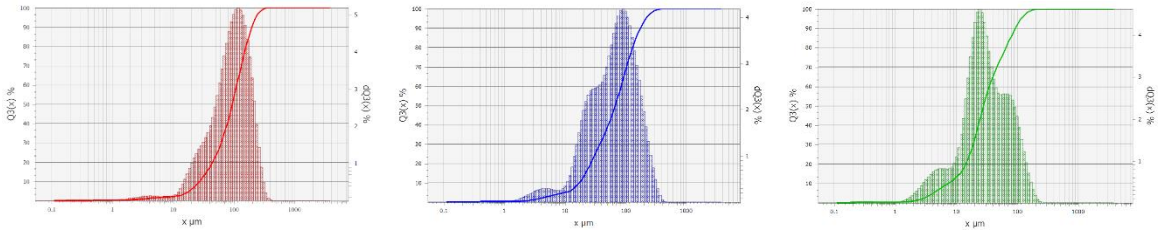

Figure 10. PSD of high-energy micromilled 14YWT powder after (a) 30, (b) 60, and (c) 100 minutes.

Table 4. Summary of PSD data for high-energy micromilled 14YWT powder.

Mass Milled(g)	Minutes Micromilled	D90 (Mean µm)	D50 (Mean µm)	D10 (Mean µm)
30	15	221.7	129.0	51.8
30	30	199.1	94.2	27.3
42	60	177.9	76.5	20.0
--	100	100	**30**	7

Since, cryomilled 14YWT powder was micromilled in a high-energy planetary mill using ceramic milling media (ZrO_2), chemistry analysis was carried out to confirm there was no change with the original alloy chemistry. ICP-MS data for micromilled 14YWT powder previously cryomilled in liquid nitrogen is shown in Table 5. Two aspects were immediately clear from the new chemical analysis, (i) there was an increase in N content, which is most likely associated with milling in liquid nitrogen, and (ii) there was a considerable presence of Zr and O, which is associated with the milling media, ZrO_2. Such a high Zr content is not ideal for a 14YWT alloy, and therefore a different particle refinement method needs to be identified. As for high N content, it may lead to precipitation of different nitride phases, which may affect mechanical properties of 14YWT alloy. After considering the chemical analysis it was determined cryomilling or high-energy micromilling using ZrO_2 media is not a suitable method to induce particle size refinement in the mechanically alloyed 14YWT ODS alloy.

Table 5. ICP-MS data, cryomilled and micromilled 14YWT powder.

ICP-MS	O	N	C	H	Fe	Cr	Y	W	Ti	Mn	Ni	Cu	Al	Si	Zr
Micromilled V540-03-40hr	0.95	0.036	0.052	0.005	81.3	13.8	0.21	2.99	0.44	0.019	0.024	0.004	0.026	0.069	1.6

Since milling using ZrO_2 media led to significant contamination of as-received 14YWT alloy powder, high-energy micromilling of initially cryomilled 14YWT powder using hardened SS media was carried out next. The first trial was performed in a ceramic vial and did not lead to particle refinement. A subsequent trial was carried out in a steel vial using hardened SS balls as the milling media. The PSD of high-energy micromilled 14YWT powder is shown in Figure 11, after 65 minutes of milling. Compared to the cryomilled condition, micromilling using SS media resulted in particle refinement. However, the refinement process kinetics are very slow, and it would require long milling times to produce particle refinement suitable for solid-state sintering. Due to the unrealistically long milling times required for particle refinement through cryomilling or high-energy micromilling, neither method is a suitable approach. Milled 14YWT powders were returned by the vendor and are currently stored at PNNL.

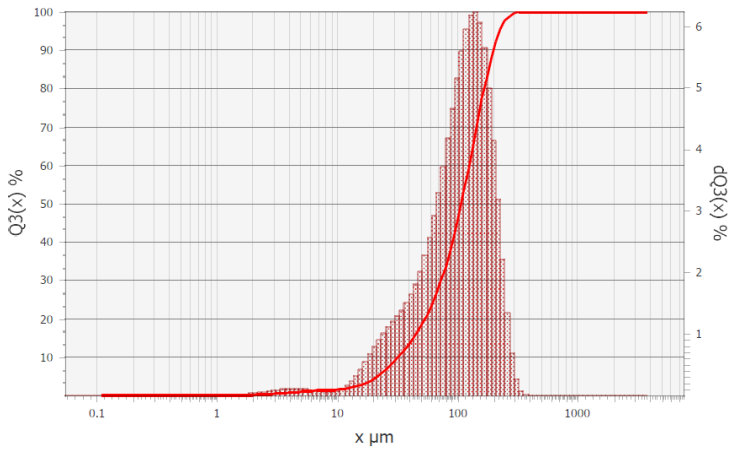

Figure 11. PSD of cryomilled and high-energy micromilled 14YWT after 65 minutes SS milling.

2.1.3.3 Sieving

The second approach to reducing the powder size was sieving using a sieve set on a shaker. A set of five sieves with a mesh size of 315, 200, 154, 43, 22 microns were placed in this order on a Rotap sieve shaker for approximately 15 minutes. Post sieving, the quantity of powder in each sieve was weighed and has been tabulated in Table 6.

Table 6. Results from sieving of as-received material.

Mesh Size	Wt% Powder, Round 1	Wt% Powder, Round 2	Wt% Powder, Round 3
>315 µm	38.07	33.62	30.97
>200 µm	29.06	28.42	28.42
>154 µm	6.67	7.45	7.58
>43 µm	23.65		
>22 µm	0.44	30.5 (<154 µm)	33.03 (<154 µm)
<22 µm	0.014		

PSD of the sieved material was measured using the Microtrac Sync particle size analyzer. The PSD of the as-received and sieved powder with diameter between 43 and 154 microns, obtained by laser diffraction technique and SEM imaging, are compared in Table 7and Figure 12. We wanted to capture powder with smallest diameter with usable quantity therefore, the second and third round of sieving was done by removing the sieves with mesh size of 43 and 22 µm. The results were similar with about 30% of powder having a diameter of 154 µm and below.

Table 7. PSD of sieved 14YWT by laser diffraction and imageJ analysis of SEM images.

PSD by volume	Size, µm Laser Diffraction	Size, µm SEM imageJ
d10	48.58	48.42
d50	73.96	72.27
d90	141.3	132.5

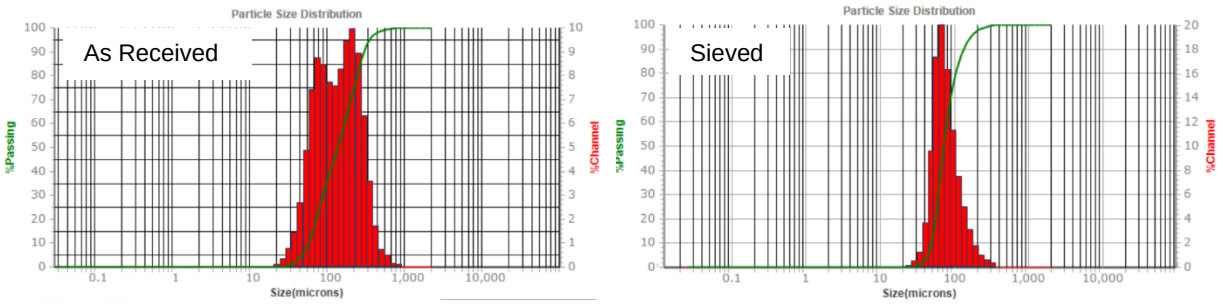

Figure 12. PSD of as-received and sieved 14YWT powder.

Figure 13a shows the SEM image of sieved 14YWT powder with diameter below 154 µm. Compared to the as-received powder, the larger particles were not observed in this case. The powder was flattened while the size was more homogenous. The size distribution was found by image analysis using ImageJ and is presented in Table 7. Sieved powder was also mounted and polished for SEM and EDS studies. SEM imaging was conducted using JEOL IT500. The SEM image of the sieved powder in Figure 13b shows the presence of flattened and deformed particles. Many of them have internal cracks and holes with W oxide at the surface of the crack (EDS elemental map in Figure 14) while some particles seemed to have welded together. Flattened particles, presence of W oxides, and internal cracks will be detrimental to densification during sintering. Powder particles also had varying grain sizes ranging from nano to micron scale as shown in Figure 13c, which may influence microstructure during sintering.

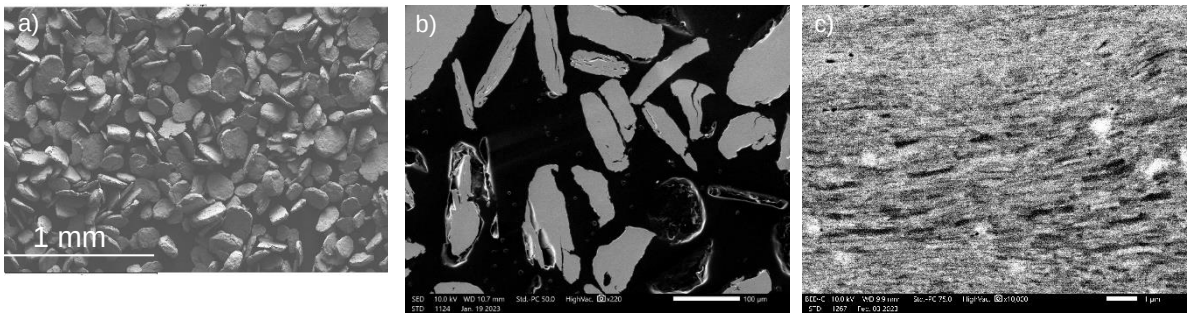

Figure 13. a) Sieved 14YWT powder particles set on tape for SEM imaging, b) sieved 14YWT powder particles mounted and polished for SEM imaging, and c) higher magnification backscatter image showing varying grain size.

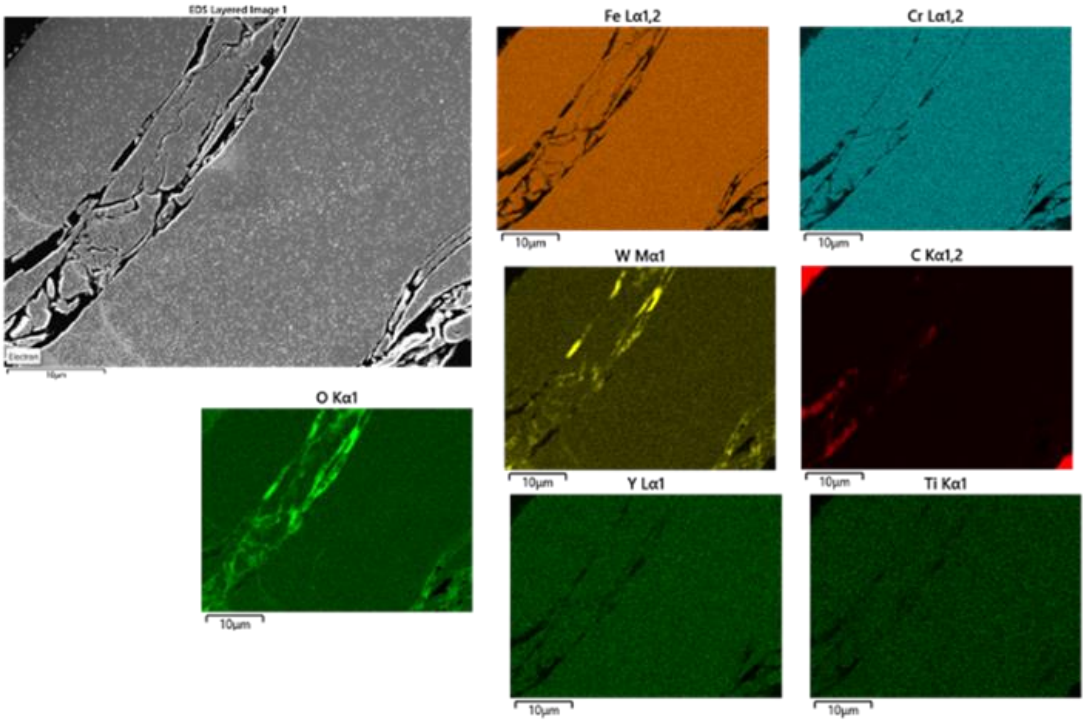

Figure 14. EDS elemental maps shows W oxide at the crack surface in mechanically alloyed 14YWT powder.

2.1.4 Filament Fabrication

The first step toward the FFF process is fabrication of filaments that are made of polymeric binder mixed with metal powder. A high metal loading by vol.% is required for 3D shape printing and subsequent densification during sintering. For our application, 55% by volume of 14YWT powder to fabricate 1.75 mm diameter composite filaments was targeted. These filaments were used during the printing step to create intended 3D shapes. Figure 8 shows the details of polymeric binder chemistry and 14YWT metal powder that was used while fabricating these composite filaments.

Table 8. Filament chemistry of filaments made with 14YWT.

Trial #	14YWT Powder Condition	Binder Chemistry, Vol.%		Additive	14YWT Metal Loading	Printability Comment
		Sacrificial	Backbone			
1	Mechanically milled, as-received, D50 = 168 micron	PW, 12%	PP, 40%	SA, 6%	42%	Not successful
2	Sieved to 100 mesh, D50 = 74 micron	PW, 11%	LDPE, 35.6%	SA, 1.7%	51.60%	Not successful

The general strategy to produce 14YWT containing filaments for FFF 3D printing involved the use of organic binders and a micro-compounding process to mix and produce feedstock. The first test involved 14YWT material received with an average particle size larger than is typically used in this process (i.e., not suitable for a complete process demonstration). Therefore, the volume loading % possible of 14YWT in the filament was much lower than if smaller particles were available. Specifically, we demonstrated feasibility of the process initially by producing a 14YWT-based filament with a volume % of 14YWT of 42%. The formulation had a

polypropylene backbone binder (39.8% by vol.), paraffin wax sacrificial binder/processing aid (11.9% by vol.), stearic acid (5.9% by vol.), and the as-received 14YWT (42.4% by vol.). This formulation was extruded twice to improve homogeneity and processed at 135°C and a screw speed of 15 rpm to yield a ~1.7 mm filament that was easy to spool and of good quality. The second trial involved a slightly reduced particle size of 14YWT that was obtained by sieving, which allowed for production of a filament material containing a metal loading of 51.6% by vol.

From Table 8, it is evident that size of the 14YWT powder plays a major role toward how much vol.% can be incorporated in the composite filament. Reduction in particle size leads to high vol.% incorporation. The polymeric binders used for making these filaments ensures good flexibility of these filaments, needed for easy storage. Successful spooling of composite 14YWT filaments is evident in Figure 15.

Figure 15. Images of composite 14YWT filaments that could be spooled.

Subsequently, cross-section imaging of these filaments was carried out in SEM to find additional details about the distribution of powders within the filament, Figure 16a shows longitudinal section of composite 14YWT filament made with as-received feedstock. The presence of irregular-shaped powder with various sizes is evident. Figure 16b shows longitudinal section image of composite 14YWT filament made with 100 mesh sieved powder. Powder size distribution is more uniform after sieving; however, the filament appears to be made up of long elongated particles, which is clear in Figure 16c. Although the 14YWT powder vol.% could be improved in the composite filament when 100 mesh sieved feedstock is used, the elongated morphology of the powder remained a concern for the success of printing 3D shapes using these filaments. Print trials were carried out with both the filaments. 42 vol.% filament did not work. For 51 vol.% loaded filament, two trials were carried out, one using 0.4 mm diameter nozzle and another using 1.0 mm diameter nozzle. Both print trials were unsuccessful due to fracture of filaments at the print nozzle, which is most likely due to the large and high aspect ratio of 14YWT powder used.

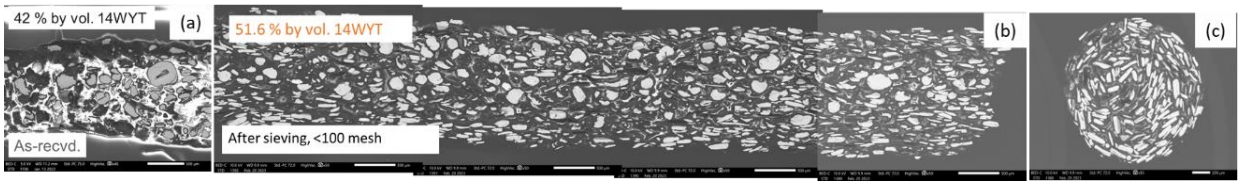

Figure 16. SEM images of composite 14YWT filament cross-section.

2.2 Experimentation on Powder 1 Batch 2

As indicated in Section 2.1, powder with platelet morphologies with a variety of size distributions did not yield filaments that were printable. Therefore, development continues using spherical powder designated as Powder 1, Batch 2 of a 325 mesh, received from Dr. T.S. Byun.

2.2.1 Characterization of 14YWT ODS Steel Powder

The powder obtained from ORNL was a gas atomized powder manufactured by Crucible Research. The composition of this alloy powder as per the manufacturer at the time of production is shown in Table 12. No additional chemical analysis has been performed on this material as part of this work, it is noted that the product likely has changed slightly and trace elements are not known but likely are those typically found in steel powders (Si, Ni, Mo, Mn, etc.).

Table 9. Chemical composition of Praxair 316H SS powder.

	Fe	Cr	W	Ti	Y
Wt%	Bal.	14	3	0.4	0.2

The as-manufactured metal powder has a nominal PSD of less than 325 Mesh or 44 µm. The particle size distribution of the 14YWT powder was measured using a Malvern MS2000 particle size analyzer coupled with a HydroS wet dispersion unit and is shown in Figure 17. One drop of surfactant (XLS 74081) was added to the mixture to help with dispersion of the fine, hydrophobic particles. The size distribution of the powder is well suited for material densification with a broad range of particles at and below the critical size range identified previously for the ODS batch 1 powder of less than 100 µm. Note the particle size distribution is on a volume basis, for such a broad tail to be identifiable on the distribution plot the number of particles 5 µm and below high allowing for closer proximity in the filament produced and subsequently greater material densification. The particle density of the ODS powder measured using a Micromeritics AccuPyc II 1340 gas pycnometer and select particle size percentiles are given in Table 10. The morphology of the 14YWT powder can be seen in Figure 18.

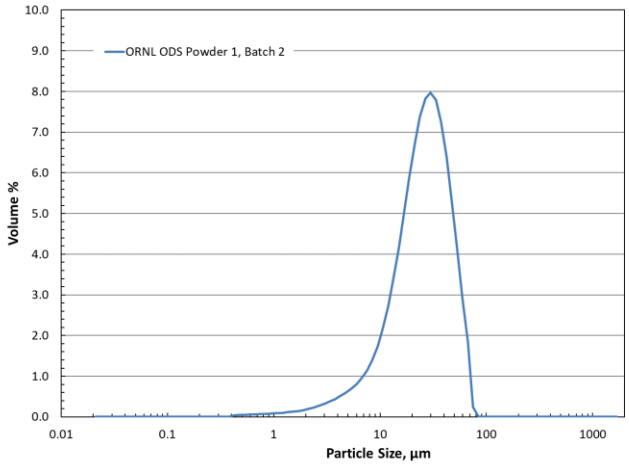

Figure 17. Particle Size Distribution of ORNL ODS 14YWT Powder

Table 10. Physical Properties of Crucible 14YWT Steel Powder

Manufacturer Information	Particle Density	Particle Size µm		
ID	g/cm^3	d10	d50	d90
14YWT Powder 1, Batch 2	7.866	10.64	28.94	55.16

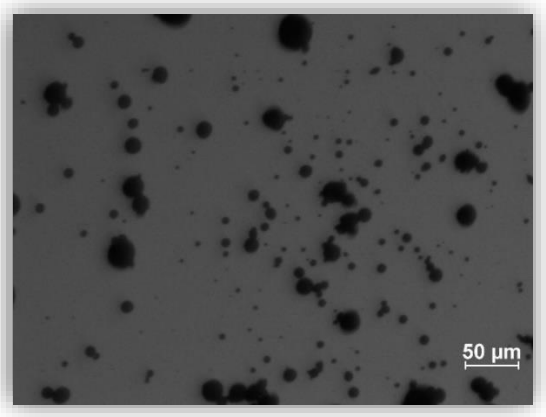

Figure 18. 14YWT ODS Powder 1, Batch 2, less than 325 mesh spherical powder obtained from ORNL.

2.2.2 Filament Fabrication

The 14YWT ODS powder was compounded using an Xplore Micro Compounder, MC 15 HT shown in Figure 19 The binding polymer mixture was compounded with the 14YWT powder at 145 °C with a screw speed of 30 rpm, until the reported torque stabilizes in the machine (for this

material, we recorded a stabilization of approximately 5 Nm for the torque). The temperature was dropped to 140 °C for the extrusion process and the screw speed was decreased to 5 rpm. The powder content of our one and only attempt at making filament was successful at 65% by volume. The resultant filament was smooth and easy to handle with a diameter of 1.62-1.70 mm (Figure 20). The filament composition is given in Table 11. An image of the cross section of the filament can be seen in Figure 20.

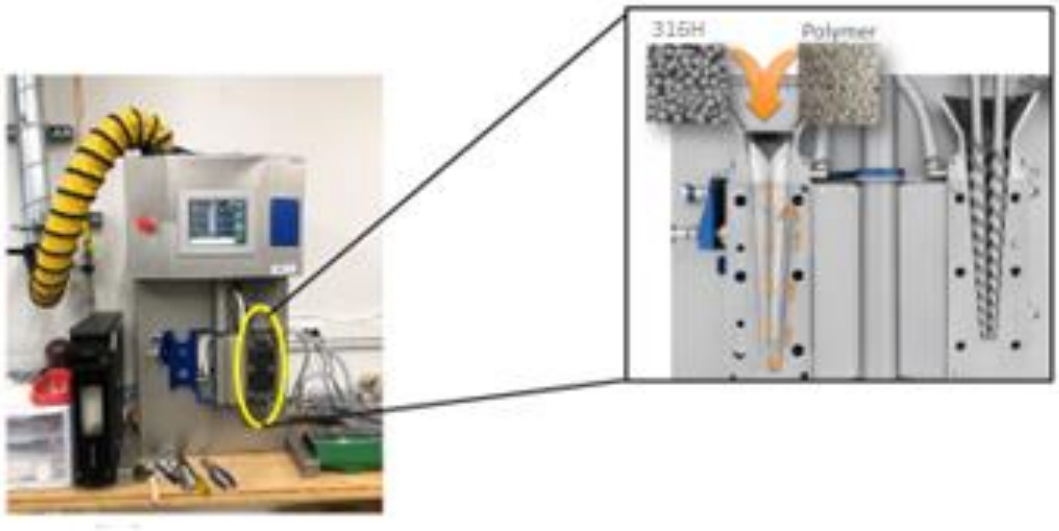

Figure 19. Xplore Micro Compounder, MC 15 HT and 14YWT Filament-65% Vol.

Table 11. 14YWT Filament Composition

Binder	**Volume %**
Polypropylene	25
Paraffin wax	8.3
Stearic acid	1.7
Metal Powder	**Volume %**
14YWT-Powder 1, Batch 2	65
Material Type	**Mass %**
Organic	6.3
Inorganic (316H)	93.7

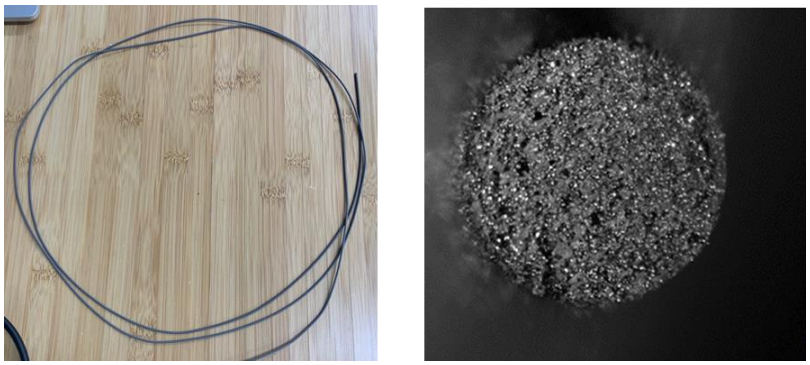

Figure 20. Filament loading 65% by volume fabricated from 14YWT 325 mesh spherical powder.

2.2.3 Printed Components and Post Treatment

The dimensions of the printed pieces are given in Figure 21 and pictures of the 3D printed parts are shown in Figure 22. Note the surface features and texture from the printing process and the poor fill of the honeycomb print, this likely could have been improved on if time allowed.

The 65% vol. loaded filament was used to successfully print 4 components (Figure 22), namely 3 rectangular pieces (called flat cubes) and 1 honeycomb structure. A custom built FFF printer was used for printing with a 0.4mm stainless steel nozzle, heated bed with a PEI plate, a BondTech Extruder and E3D heater block and heat sink. Repetier Host was used as the printer interface program and a custom set of slicing parameters were set through the slicing software Slic3r.

Filament Settings:

- Nozzle Temp: 185 °C
- Bed Temp: 60 °C
- Nozzle: 0.4 mm stainless steel
- Extrusion Multiplier: 1.1
- Diameter: 1.6 mm

Print Settings:

- Layer Height: 0.15 mm
- Infill: 100%
- Speed: 5 mm/s
    - For **Flat Cube** prints: 1 perimeter and 2 top/bottom solid layers.
    - For **Honeycomb** prints: 2 perimeters and 2 top/bottom solid layers.

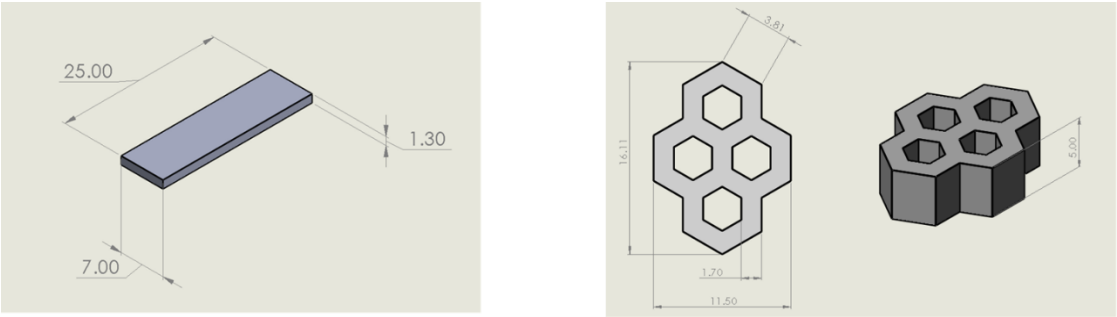

Figure 21. Dimensions of the Flat Cube and Honeycomb Print Forms Printed

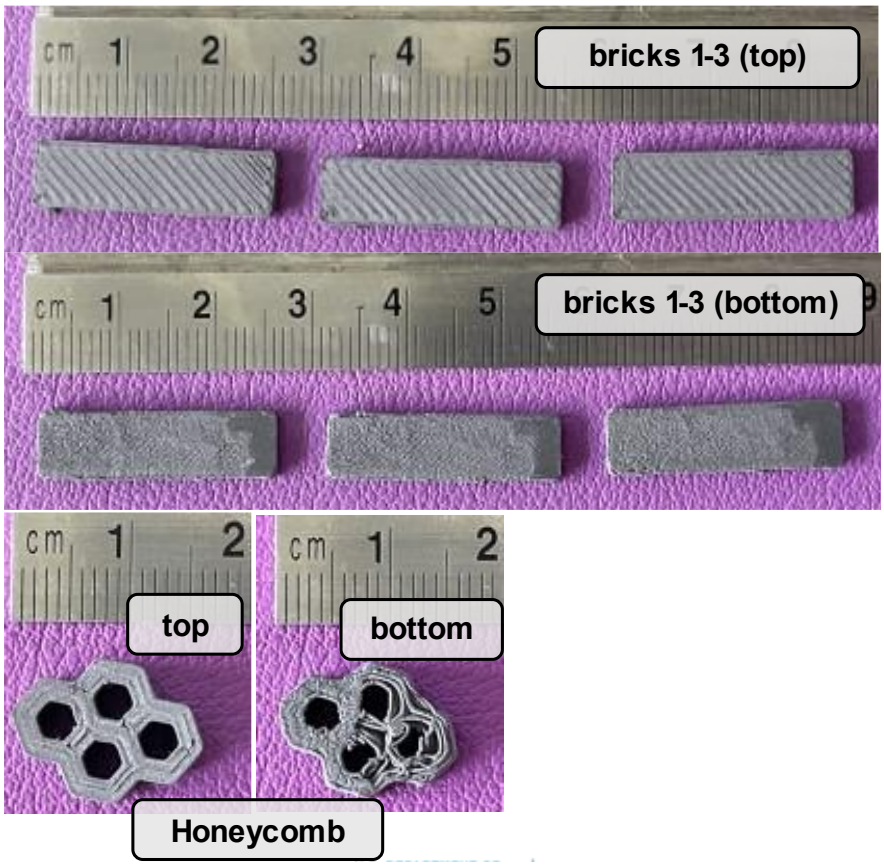

Figure 22. The 65% vol 14YWT ODS Filament as Printed (with Binder).

2.2.4 Post Processing (removal of binder)

Prior to sintering the metal prints the binder material (Table 11) needed to be chemically removed from the printed forms. This process, referred to as solvent debinding, required a static soak in cyclohexane at slightly elevated temperature (42 °C) for approximately 24-36 hrs. The pieces were then rinsed with fresh cyclohexane and dried, ready for thermal debinding. Thermal debinding was coupled with the sintering process discussed in the next section. The first part of the sintering process included a very slow ramp from room temperature with holds at 450 and 600 °C to allow any residual polymeric binder material to slowly diffuse out of the printed parts. Again, due to our limited resources, we selected a conservative, slow ramp and hold program to increase our chances of success. Our first and only attempt at sintering was successful, where success is defined by the fact that none of our printed parts exploded during sintering. If residual binder material persisted in the printed forms upon heating to the sintering temperature, they would have exploded. We thermally debound and sintered 2 printed pieces, one flat cube and the honeycomb.

The thermal debinding protocol used in this study were:

- Ramp: room temp to 450 °C @ 1 °C/min
- Hold: 3 hours at 450 °C
- Ramp: 450 C to 600 C @ 1 °C/min
- Hold: 3 hours at 600 °C

2.2.5 Sintering

Sintering was performed on 2 of the 4 printed pieces, pieces with duplicates were not sintered, allowing us to modify if needed thermal debinding protocol and/or sintering temperature. After performing a limited literature search a conservative thermal debinding and sintering protocol was established. A CM Hydrogen atmosphere batch furnace system, Model # 1516GSH2FL was used for the sintering process with the program listed below.

Sintering protocol

- Purged with Argon
- Start H_2 flow
- Ramp: room temp to 450 °C @ 1 C/min
- Hold: 3 hours at 450 °C
- Ramp: 450 C to 600 °C @ 1 C/min
- Hold: 3 hours at 600 °C
- Ramp: 600 C to 1360 °C @ 5C/min
- Hold: 2 hours
- Cool: 1-10 °C /min dependent on furnace capability
- Purge with Argon

Figure 23. CM Hydrogen Atmosphere Batch Furnace

As previously discussed, the thermal debinding of the parts occurs at the lower temperatures to remove residual organic binding material not removed during chemical debinding to avoid potential form deformation or rupture. After thermal debining the printed parts were then brought up to temperature gently at a rate of 5 °C/min to the selected sintering temperature of 1360 °C, where they were held for 2 hours. Due to time and budget constraints only one sintering temperature was explored, it may be advantageous to explore other temperatures in the future.

2.2.6 Microstructural Analysis of 14YWT ODS Steal Component Fabricated by Spherical Powder

Images of the sintered parts were taken with a Keyence High Performance VHX-7020 optical microscope to observe the overall structure. The side profiles, A and B and top and bottom (Figure 24 and Figure 25). Additional high-resolution imaging of the surface of the sintered materials was performed using a JEOL 7001F LV scanning electron microscope (SEM) equipped with dual energy dispersive spectrometers (EDS), and energy backscatter diffraction

(EBSD). Micrographs shown in Figure 25 exhibit densification at the central region (A, B) and more void space toward the edge of the material (C, D). Similarly, we can see that we observe increased densification of the honeycomb shape in the center of the printed piece, it is worth noting the honeycomb piece was 5 mm thick while the flat cube was only 1.3 mm thick. We can see in Figure 27 the densification of the honeycomb piece is increased at the center regions.

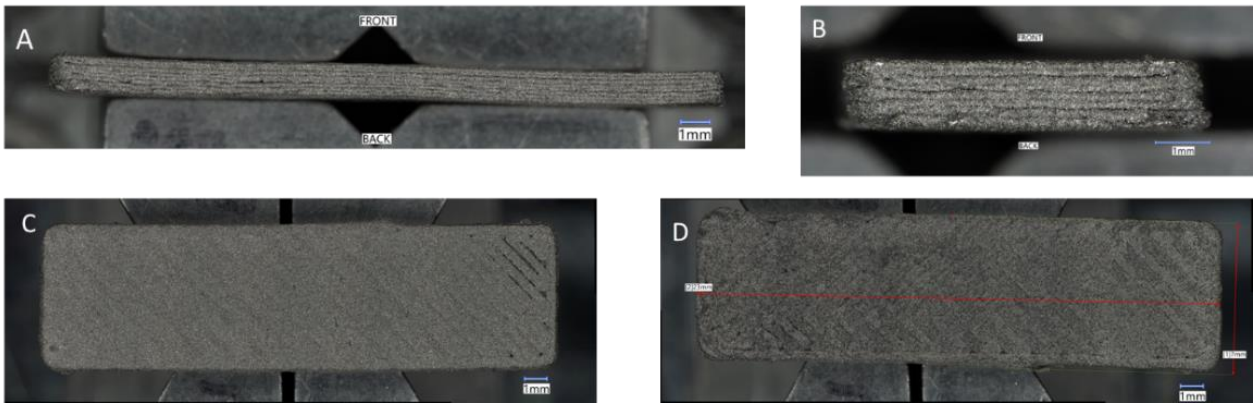

Figure 24. Images of Sintered Flat cube of 14YWT ODS Printed Filament, 65V%

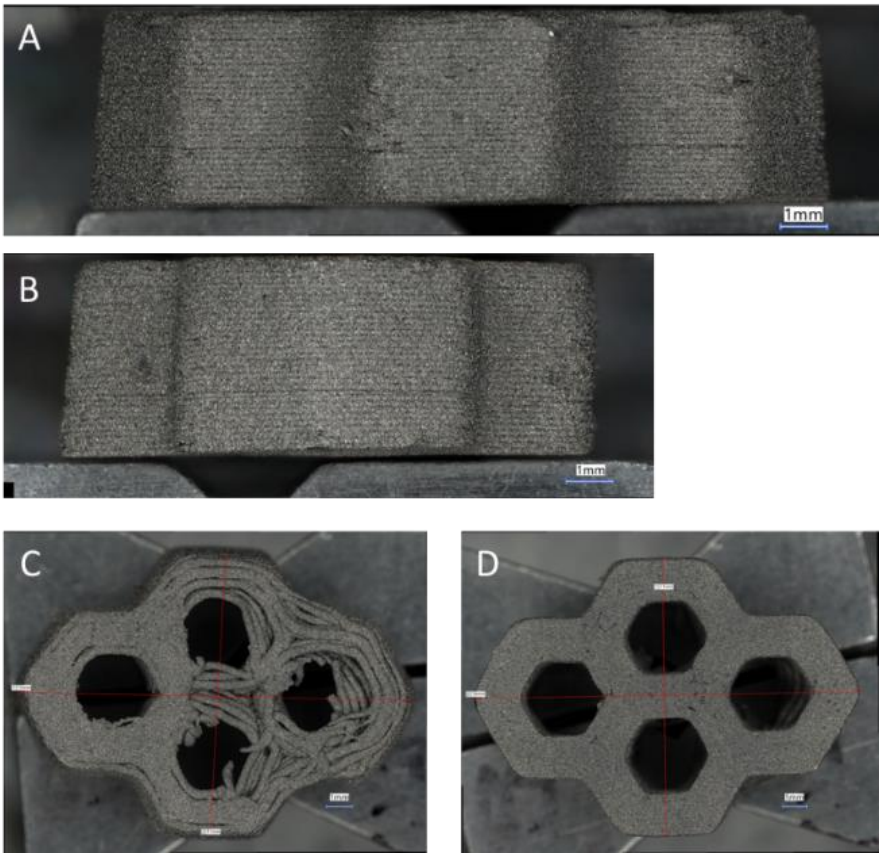

Figure 25. Images of Sintered Honeycomb of 14YWT ODS Printed Filament, 65V%

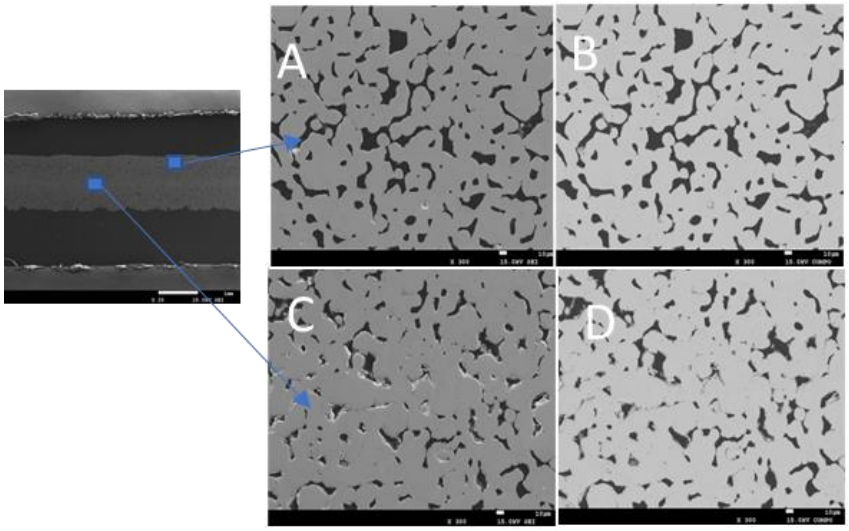

Figure 26. Flat Cube Cross Sectional Sample. Wall regions (A, B) and central region (C, D).

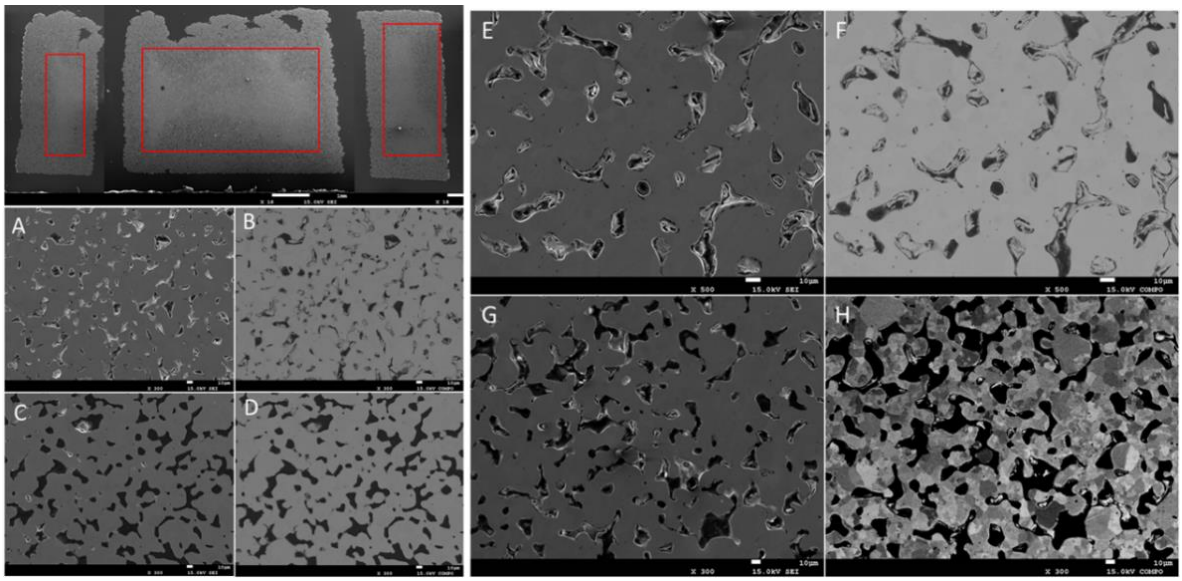

Figure 27. Honeycomb Cross section Micrographs collected using BASE and SEI. A, B and E, F, center regions, C, D and G, H edges.

2.3 Feasibility of FFF for Fabrication of ODS Steels

The research results provided in this report are evidence that it is feasible to print ODS steel using solid-state FFF process with the following conclusions:

- The filament fabrication process and printing thereof are sensitive for the powder morphology, size, and size distribution mainly due to the flowability of the filament extrusion as well as the sinter effectiveness.
- Custom powder can be used for FFF; therefore, an in-house PNNL capability was developed enabling ODS powder loading technique.

3.0 Feasibility of FFF for Fabrication of 316SS

As in the case with the ODS powder, two 316SS batches were used for the development work and feasibility for utilization of the FFF process. Previous research by PNNL on 316L and with commercial filaments were successfully executed as part of another project, but 316H and custom-made filaments were addressed as part of this study. Although both powder batches investigated were spherical, the initial powder batch used was typically sized for direct energy deposition manufacturing processes and the second batch was 15–45 µm. As with the initial lessons learned as part of the ODS FFF experiments, only one experiment on the larger powder was attempted and the filament fabrication was deemed unsuccessful. Therefore, the rest of this section will report on the smaller powder size development results.

3.1 Characterization of 316H SS Powder

A sample of Praxair product number Fe-455-N30 316H SS powder was provided to PNNL by Argonne National Laboratory (ANL). This material was procured by ANL in November 2022. The chemical composition of this 316H SS powder is shown in Table 12. This analysis was provided by the vendor on shipment and was performed in October 2022. No additional chemical analysis has been performed on this material as part of this work.

Table 12. Chemical composition of Praxair 316H SS powder.

	Fe	Cr	Ni	Mo	Mn	Si	C	O	N	P	S
Wt%	Bal.	16.8	12.1	2.5	1.13	0.48	0.06	0.03	0.01	<0.005	0.00

The as-manufactured metal powder has a nominal PSD of 15–45 µm. The material shipped to PNNL was “recycled” from metal powder printing activities performed at ANL, the powder was reclaimed and passed through a 63 µm sieve. The PSD of the 316H powder measured using a Malvern MS2000 particle size analyzer coupled with a HydroG wet dispersion unit is shown in Figure 28.

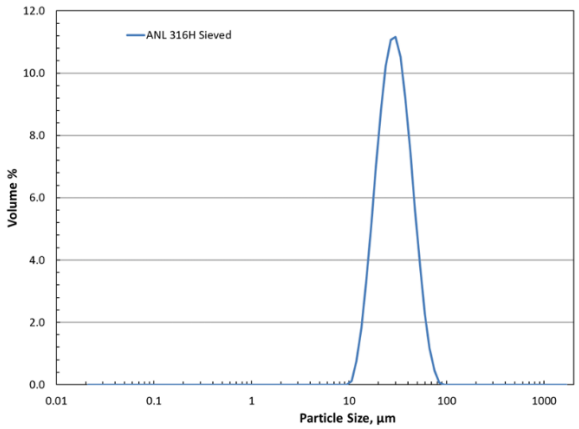

Figure 28. PSD of as-received Praxair 316H SS powder.

The physical properties of the Praxair 316H SS powder is summarized in Table 13. Previous experience from exploring ODS materials for similar applications determined that a starting particle size of less than 100 µm was more likely to result in a workable filament. A narrow PSD would also influence the microstructure of the 316H during sintering, possibly decreasing the

occurrence of abnormal grain growth and recrystallization. A uniform particle size and morphology minimizes grain-to-grain variation increasing the densification of the final sintered product.

Table 13. Physical properties of Praxair 316H SS powder.

Manufacturer Information	Particle Density	Apparent Density	Tap Density	Particle Size (µm)		
Product ID	g/cm^3	g/cm^3	g/cm^3	d10	d50	d90
Fe-455-N30	7.97	4.39	5.00	19.6	32.3	53.6

The morphology of the 316H SS powder can be seen in Figure 29. The powder is spherical in nature, with many particles that are highly spherical, which is expected from particles produce from thermal spray techniques. The metal powder has several elliptical particles and small fused particles and texture on the surface of larger particles. The size ranges observed are consistent with the PSD obtained from laser diffraction. It should be noted that laser diffraction struggles to accurately measure PSDs that span several orders of magnitude, and the size distribution is measured and reported on a volume basis. The presence of small particles, as seen in Figure 29, of approximately 1–5 microns, are not observed on the PSD shown in Figure 28 due to their low volume concentration relative to the larger particles present.

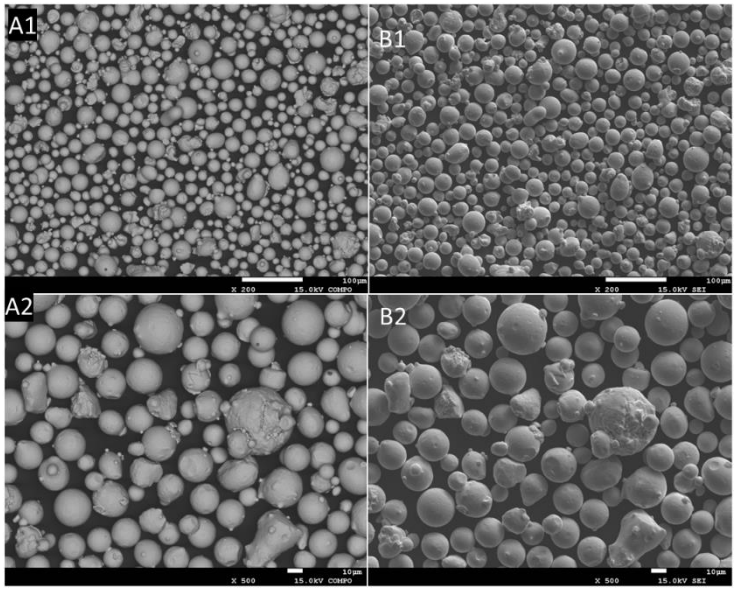

Figure 29. Observations of 316H SS powder using SEM in both secondary (A1, A2) and backscatter (B1, B2) imaging modes. Micrographs exhibit spherical particles with texturing on the surface. Nonuniform particle distributions were observed (>10 um to 40 um).

3.2 Filament Fabrication Using 316H SS

The 316H SS powder was compounded using an Xplore Micro Compounder, MC 15 HT, shown in Figure 30. The binding polymer mixture was compounded with the 316H powder at 145°C with a screw speed of 30 rpm, until the reported torque stabilized in the machine (for this material, we recorded a stabilization of approximately 9 Nm for the torque). The temperature was dropped to 138°C for the extrusion process and the screw speed was decreased to 10 rpm. Initially we attempted to incorporate 65 Vol% metal powder unsuccessfully, the resultant

filament was brittle and unsuitable for our purposes (3D printing). Decreasing the metal powder loading to 62 Vol% resulted in a filament that was smooth and easy to handle with a diameter of 1.62–1.70 mm. The final filament can be seen on the lower right of Figure 30.

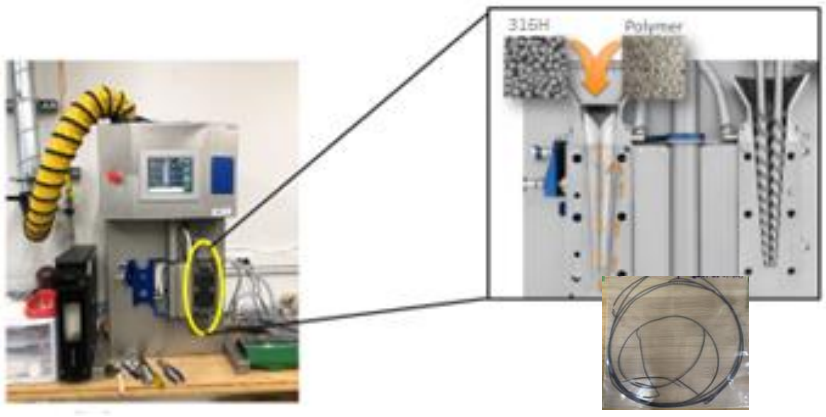

Figure 30. Xplore Micro Compounder, MC 15 HT, and 316H filament with 62 Vol%.

The filament composition and binder materials used in volume percent are given in Table 14, along with the mass percent breakdown of inorganic (316H steel powder) and organic material.

Table 14. Filament composition.

Binder	**Volume %**
Polypropylene	27.1
Paraffin wax	9
Stearic acid	1.9
Metal Powder	**Volume %**
316H	62
Material Type	**Mass %**
Organic	6.4
Inorganic (316H)	93.6

Images of the filament were taken with a Keyence High Performance VHX-7020 Microscope and JEOL 7001F LV SEM, images to evaluate the particle packing and uniformity of the filament are shown in Figure 31. From the higher resolution microscope images, it appears that the surface of the filament is evenly filled with metal powder with no obvious spaces lacking in metal particles. At the much higher magnifications of the SEM, 100x to1000x, it is observed that there are areas that have lower concentrations of metal particulate. The cross-sectional view of the filament, Figure 31 (G-I), reveals areas of lower particle density and in some cases void of particles. It also appears that the particles are less spherical, have small flat regions, and an increase in debris material can be observed which is a result of the tortuous compounding process. The uniformity of the binder/metal compound greatly influences the final product in AM and these low powder areas will likely result in a void space post-sintering. The diameter of the filament appears to be very regular with slight surface variations only visible with the aid of a microscope. SEM images enable us to visualize the packing of the metal particles within the filament. The particle packing influences the microstructure of the 316H during sintering, final void space of the sintered metal, and subsequently the mechanical properties.

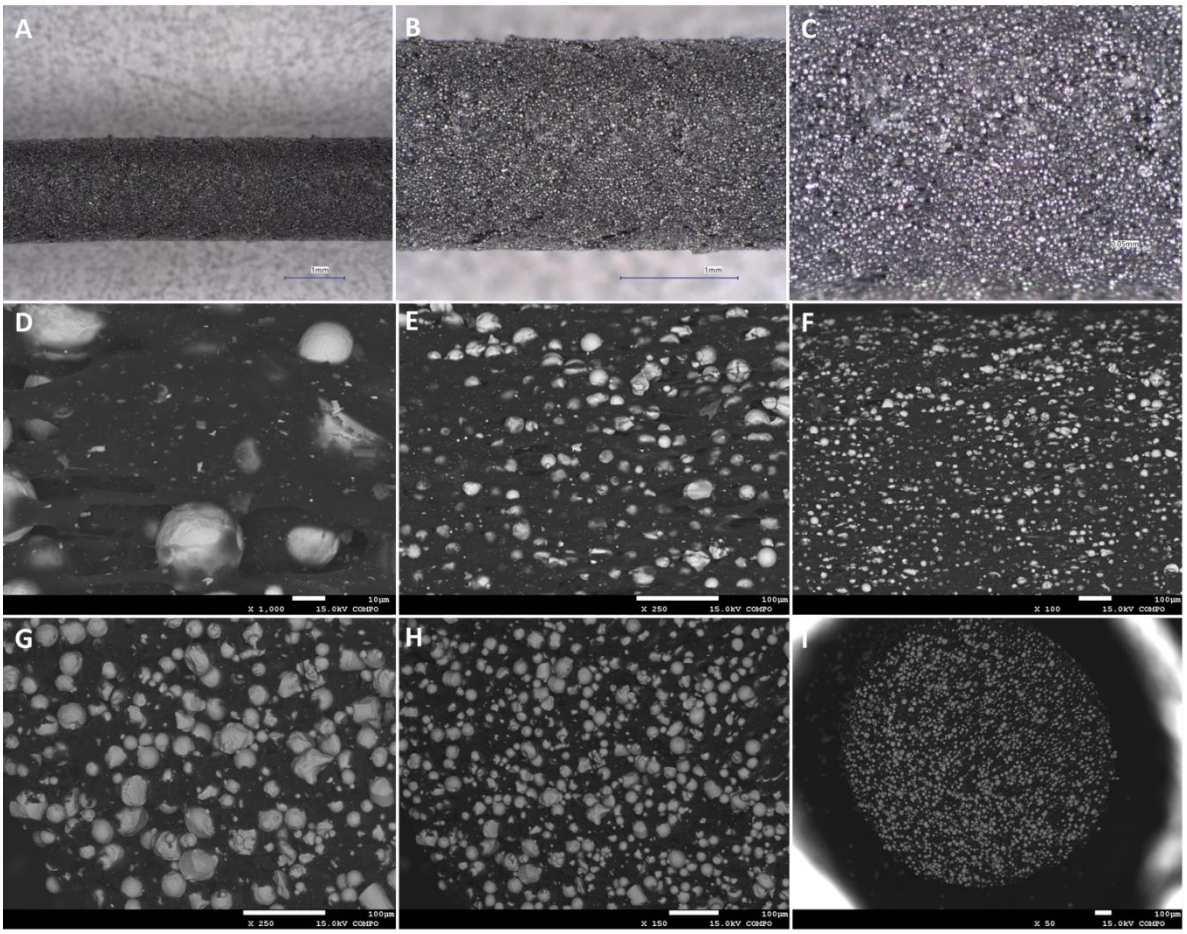

Figure 31. Images generated using optical microscopy and SEM of 62 Vol % 316H filament. Optical microscopy was used to observe the surface along the length of the wire (A-C). SEM micrographs were collected at various magnifications along the length of the wire (D-F) and cross-sectional direction (G-I).

A small section of the filament was analyzed with electron dispersive X-ray spectroscopy (EDS) and is shown in Figure 32. Except for silica, the elements of interest listed in Table 12 present in the 316H SS powder (Fe, Cr, Ni, Mo, O), follow the particle concentration. Silica appears present as a contaminant and follows the metal particles. Select elements (S, N, Mn, P) were excluded from EDS analyses due to peak intensity overlap and low concentrations of light elements not suitable for EDS.

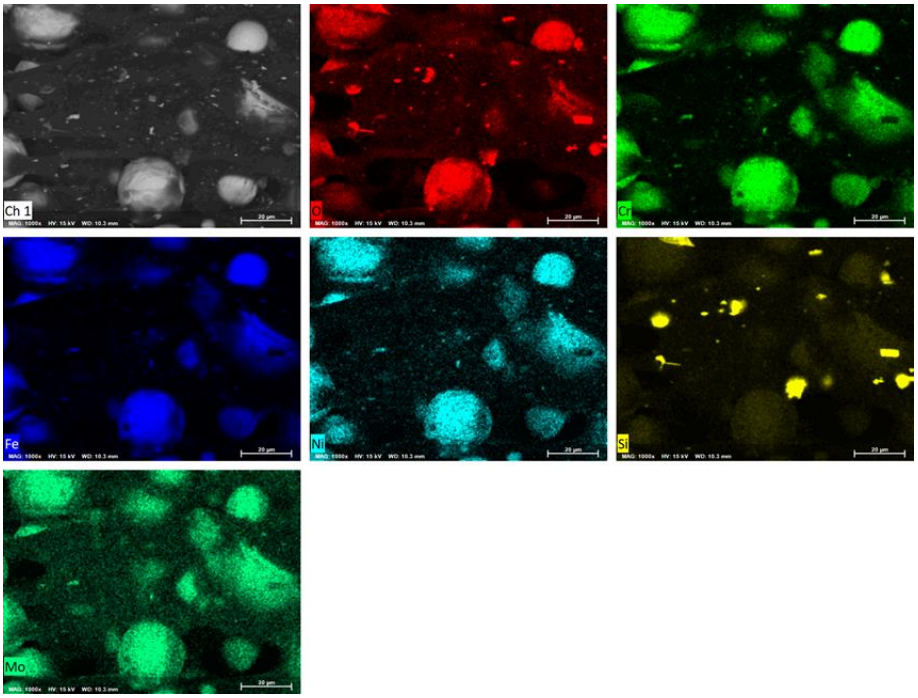

Figure 32. Elemental maps generated using EDS for as-fabricated wire sample. Selected elements (S, N, Mn, P) were excluded due to peak intensity overlap and low concentrations of light elements not suitable for EDS analysis.

3.3 3D Printing and Post-Processing of 316H SS

3.3.1 Printing

A custom-built FFF printer shown in Figure 33 was used for printing with a 0.4 mm SS nozzle, heated bed with a PEI plate, a BondTech extruder, and E3D heater block and heat sink. Repetier Host was used as the printer interface program and a custom set of slicing parameters were set through the slicing software Slic3r.

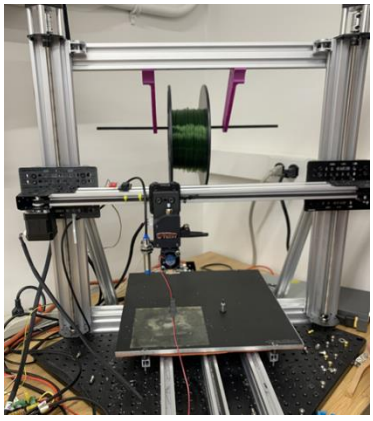

Figure 33. Custom-built FDM printer with PEI plate and BondTech extruder.

Two forms were printed to test the printability of the filament produced, a flat cube and a honeycomb. Prints were made with and without perimeters with either 95 or 100% rectilinear

infill, printed at a 45/45 orientation. Infill is the amount of material that occupies the internal part of the printed piece. A 100% infill has an internal structure that is solid and a part with 95% infill is 5% hollow. It is difficult to visually differentiate between 100% and 95% infills, but incorporating small voids throughout the part can impact sintering based on observations from our previous work on metal FFF printing. Incorporating perimeters into the part is a much larger change in part creation, as seen in Figure 34 -316H_9 shows a 3D printed honeycomb with two perimeters (which for this part size and design, resulted in a lack of infill between perimeters given the other slicing software settings). Figure 34 -316H-10 depicts a 3D printed honeycomb with no perimeters (infill only). Incorporating perimeters allows for better shape retention and dimensional control in the final part, whereas removing the perimeters to have only infill allows gases generated during the sintering process to exit the part more readily and potentially results in higher densification of the part.

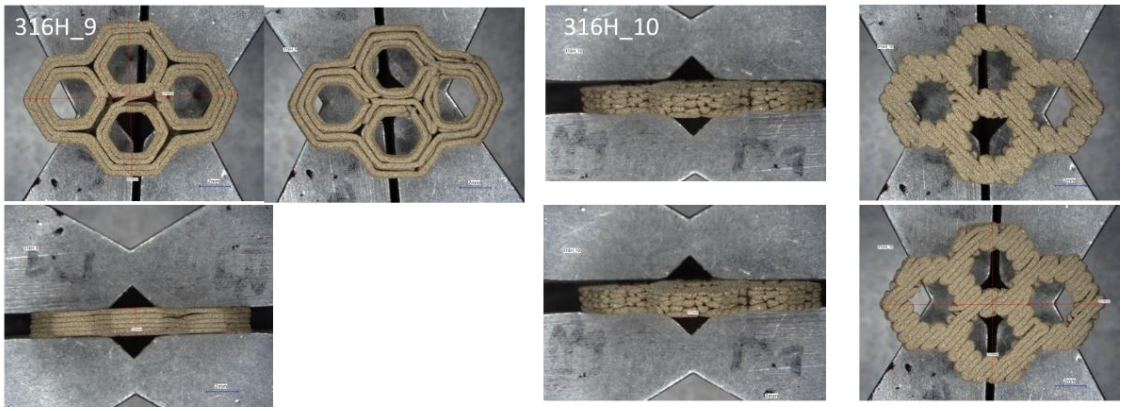

Figure 34. Impact in Printing Parameters on Print Quality

Due to budgetary constraints, optimization of print parameters was very limited. The settings used for filament extrusion and printing are outlined below. It was noted that the filament appeared to be robust, was easily handled without breaking, and even required some effort to break off sections for printing. The first extrusion test determined the filament extruded well at 185°C with no stringing or excess flow. It was also noted the 0.4 mm strand produced was flexible. Given the success of the extrusion test, this was the nozzle temperature selected for all prints presented here.

- Filament Settings
  - Nozzle Temp: 185°C
  - Bed Temp: 60°C
  - Nozzle: 0.4 mm stainless steel
  - Extrusion Multiplier: 1.1
  - Diameter: 1.6 mm
- Print Settings
  - Layer Height: 0.3 mm
  - Infill: 95 or 100%
  - Speed: 5 mm/s

- For flat cube prints: one perimeter when a perimeter was printed and two top/bottom solid layers.
- For honeycomb prints: two perimeters when a perimeter was printed with two top/bottom solid layers.

The top and bottom layers were 100% infilled while the layers between the top and bottom had the infill denoted for the print part given in Table 15. All other settings were default Slic3r settings.

Table 15. Summary of printed pieces.

Print Number	Form	Infill, %	Perimeter
1-Failed	Flat cube	95	No
2	Flat cube	100	No
3	Flat cube	95	Yes
4-6	Flat cube	100	Yes
7-9	Honeycomb	100	Yes
10	Honeycomb	100	No

For future work it would be advantageous to increase the thickness of the printed parts and optimize the print speed since this was not explored and can greatly impact the print quality of the final product.

Two print forms were printed for this study, a flat cube and a honeycomb structure to evaluate the print quality of the filament produced and the final form of the printed piece post-processing and sintering. A total of nine pieces were successfully printed, five flat cubes and four honeycombs. A summary of the infill and perimeter information for each form is given in Table 15. The dimensions of the printed forms are like those given in the previous section, see Figure 21. Parts printed with the 316H SS had slightly different thicknesses, the flat cubes are 2 mm thick, and the honeycomb is only 1.5 mm thick compared to 1.3 and 5 mm for the 14YWT ODS prints above.

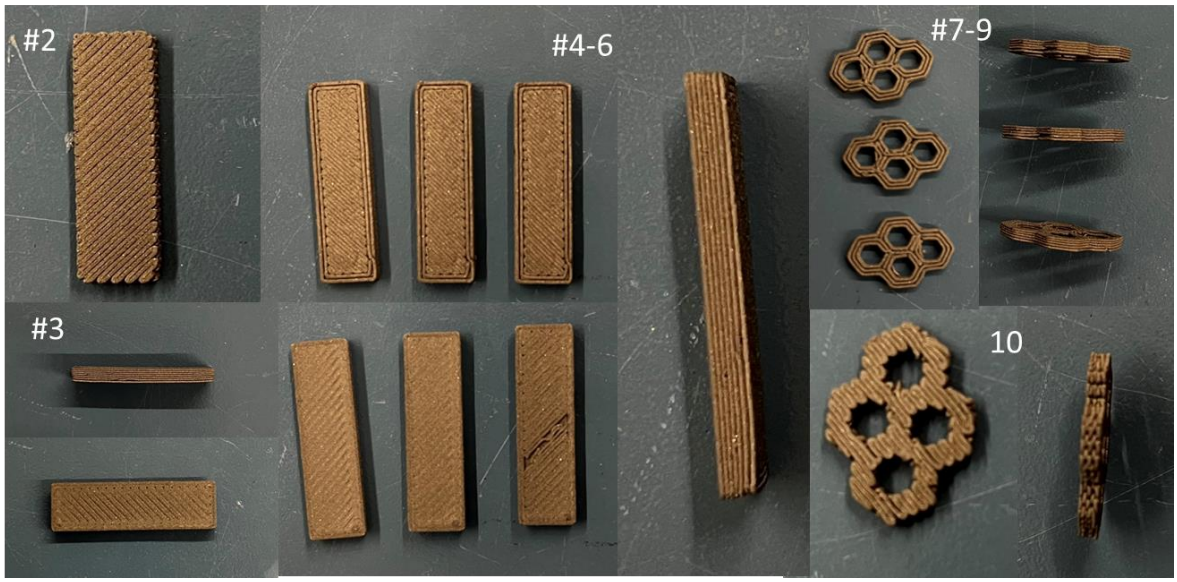

Figure 35. Images of Green Print Pieces

3.3.2 Post-Processing Removal of Binder

Prior to sintering the metal prints, the binder material (Table 14) needed to be chemically removed from the printed forms. This process, referred to as solvent debinding, required a static soak in cyclohexane at a slightly elevated temperature (42°C) for approximately 24–36 hours. The pieces were then rinsed with fresh cyclohexane and dried, ready for thermal debinding. A comparison of select green parts (as printed) and chemically debound parts is shown in Figure 36. The thermal debinding was coupled with the sintering process discussed in the next section. The first part of the sintering process included a very slow ramp from room temperature with holds at 450°C and 600°C to allow any residual polymeric binder material to slowly diffuse out of the printed parts. Again, due to our limited resources, we selected a conservative slow ramp and hold program to increase our chances of success. Our first and only attempt at sintering was successful, where success is defined by the fact that none of our printed parts exploded during sintering. If residual binder material persisted in the printed forms upon heating to the sintering temperature, they would have exploded. We thermally debound and sintered print numbers 2, 3, 6, 9, and 10 and recovered all five prints intact at the end of sintering.

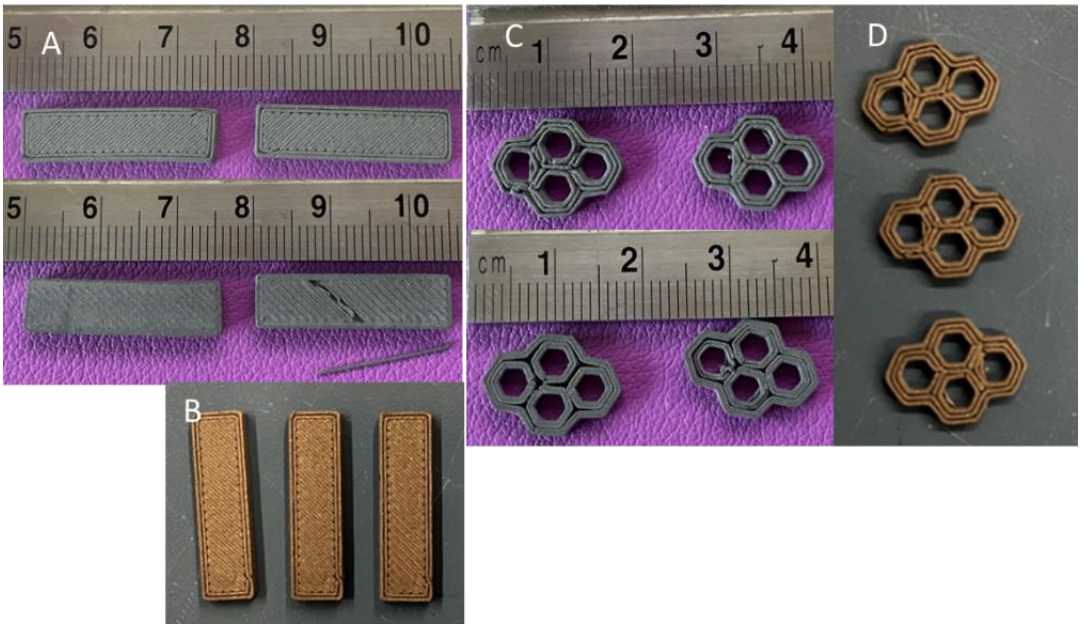

Figure 36. Select Green Parts (B and D) and Chemically Debound Parts (A and C)

The thermal debinding protocol used in this study was:

- Ramp: room temp to 450°C @ 1°C/min
- Hold: 3 hours at 450°C
- Ramp: 450°C to 600°C @ 1°C/min
- Hold: 3 hours at 600°C

3.4 Sintering

Sintering was performed on five of the nine printed pieces (pieces with duplicates were not sintered), allowing us to modify thermal debinding protocol and/or sintering temperature if needed. After performing a limited literature search, a conservative thermal debinding and sintering protocol was established. A CM Hydrogen atmosphere batch furnace system, model 1516GSH2FL, as shown in Figure 37, was used for the thermal debinding and sintering process with the complete program listed below.

Sintering protocol-Parts sinter: 2, 3, 6, 9 and 10

- Purged with Argon
- Start H_2 flow
- Ramp: room temp to 450°C @ 1°C/min
- Hold: 3 hours at 450°C
- Ramp: 450°C to 600°C @ 1°C/min
- Hold: 3 hours at 600°C
- Ramp: 600°C to 1360°C @ 5°C/min
- Hold: 2 hours
- Cool: 1-10°C/min dependent on furnace capability
- Purge with argon

Figure 37. CM Hydrogen atmosphere batch furnace.

As previously discussed, the thermal debinding of the parts occurred at the lower temperatures to remove residual organic binding material not removed during chemical debinding to avoid

potential form deformation or rupture. After thermal debinding, the printed parts were brought up to temperature gently at a rate of 5°C/min to the selected sintering temperature of 1360°C, where they were held for 2 hours. Due to time and budget constraints only one sintering temperature was explored; it may be advantageous to explore other temperatures in the future.

3.5 Microstructural Examination of Sintered 316H SS

Images of the sintered parts were taken with a Keyence High Performance VHX-7020 optical microscope to observe the overall structure. Additional high-resolution imaging of the surface of the sintered materials was performed using a JEOL 7001F LV SEM equipped with dual EDS, and energy backscatter diffraction (EBSD). A multimodal investigation of the microstructure and elemental distributions were performed on polished cross-sections and focused primarily on print numbers 6 and 10 (Figure 38 though Figure 40). The selected samples were prepared in epoxy and polished for high-resolution characterization and analysis in both the planar and cross-sectional directions to better understand the microstructure, void space, and interface of the deposited layers. Image analysis on the remaining samples (2, 3, and 9) were carried out on the as-fabricated forms and are reported in 5.0Appendix A.

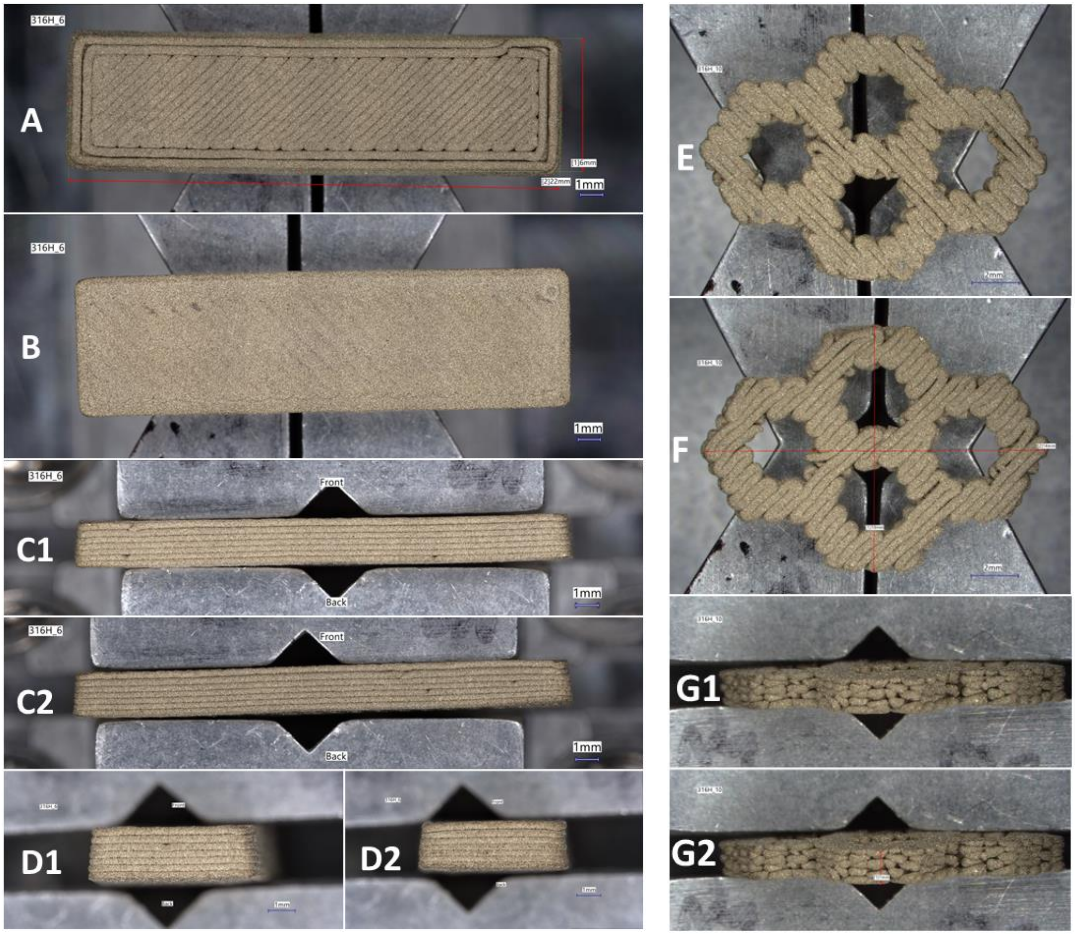

Figure 38. Image analysis on the sintered part using optical microscopy of Print 6-Flat Cube (A-D) and Print 10-Honeycomb (E-G) at different orientations: top (A, E), bottom (B, F), long side (C1, C2, G1, G2), and short side (D1, D2).

The as-sintered surface characteristics of the printed forms are given in Figure 38 through **Error! Reference source not found.** using various magnifications using backscatter (A1-A3) and secondary imaging modes (B1-B3). This informs us on the surface characteristics, topology, particle fusing, and gross void spaces.

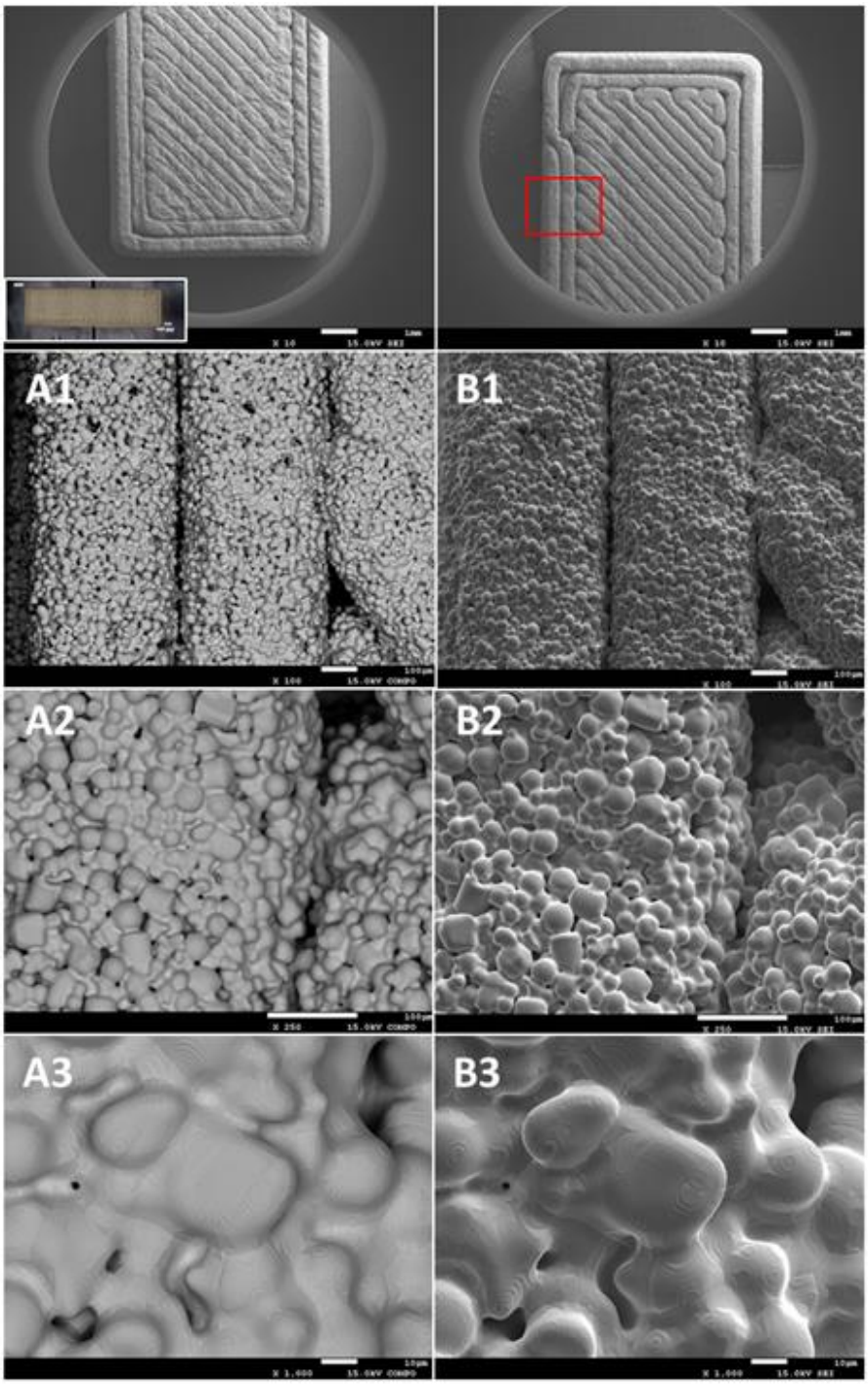

Figure 39. Image analysis at edge of as-fabricated Print 6-Flat Cube (red box). Observations at various magnifications using backscatter (A1-A3) and secondary imaging modes (B1-B3).

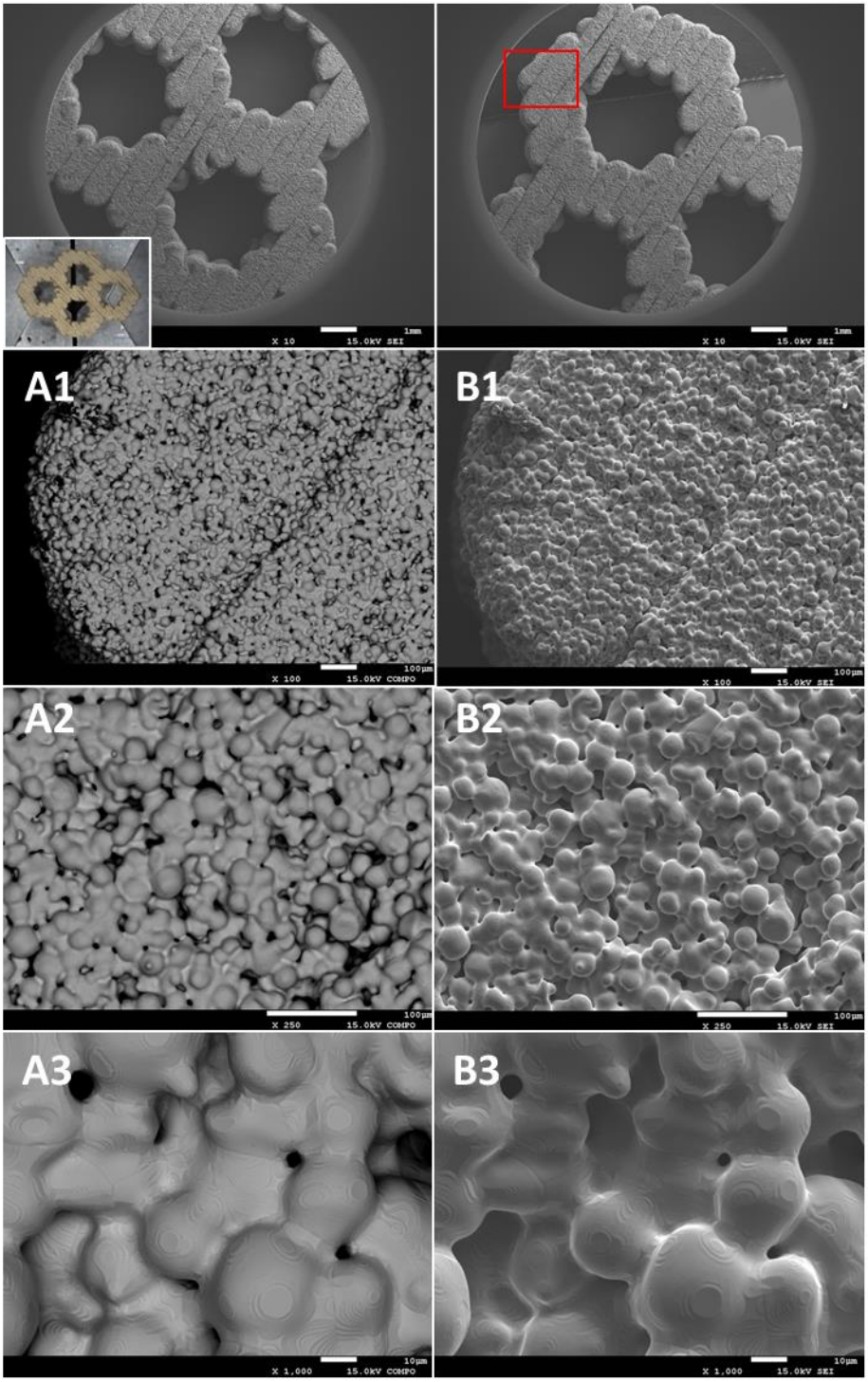

Figure 40. Image analysis at corner of as-fabricated Print 10-Honeycomb (red box). Observations at various magnifications using backscatter (A1-A3) and secondary imaging modes (B1-B3).

Figure 41 shows BSE and SEI SEM images near an edge and near the center of sintered Print #6 sample surface. The sample consisted of dense microstructure at both near edge and center

regions of the sample, suggesting a considerably high sample density. Some pore character is also observed in the sample, while it is only slightly lower at the center compared to the edge of the sample. The cross-sectional view of the sample also showed some pore character, while no significant difference between the sample surface or planar view and cross-sectional view is apparent. Spacing along interface of two depositional paths can also be observed in these SEM images.

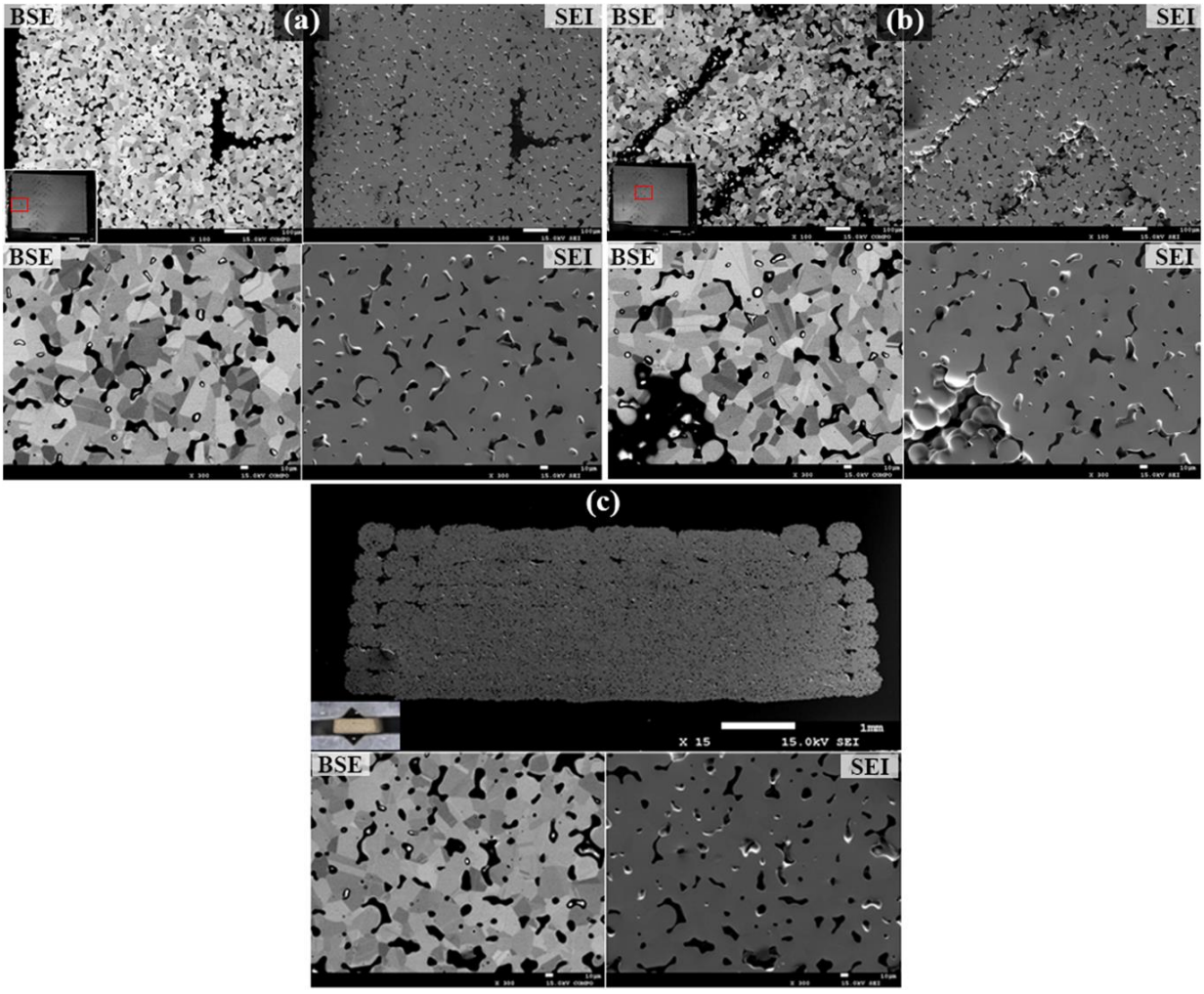

Figure 41. SEM micrographs of sintered Print #6. Planar views (left) near left edge and (right) center of the sample and (bottom) cross-sectional images. A and b show BSE and SEI mode images, respectively.

Similar to Print #6, the honeycomb Print #10 also showed dense microstructure in both the sample surface and along its cross section. These are shown in Figure 42. Interfaces between deposited layers are also apparent in these samples. Additional high-magnification micrographs are provided in Appendix A.

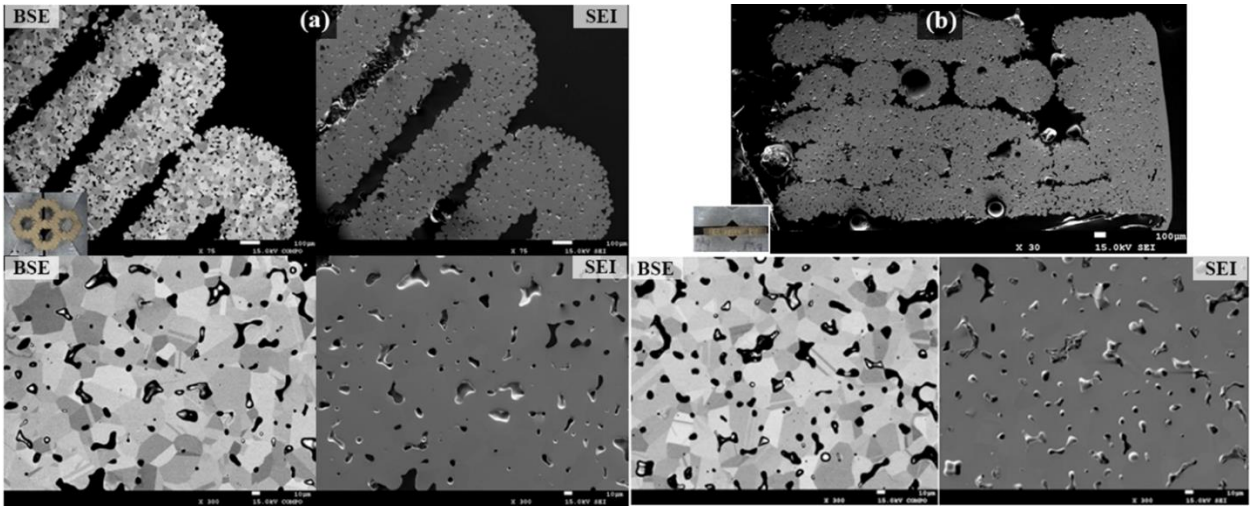

Figure 42. SEM micrographs of sintered Print #10. Planar views (left) and (right) cross-sectional images. A and b show BSE and SEI mode images, respectively.

3.6 Feasibility of 316H SS Using FFF Process

The research showed that 316H filament can be custom made achieving an initial powder loading of 62% and sintered products in rectangular and honeycomb structures were fabricated. Although effective printing and subsequent sintering did occur, further optimization is needed to fully fabricate structurally sound components. Powder size was again identified as a critical parameter for successful filament fabrication and printing with these custom filaments.

4.0 Conclusions and Recommendations

This study provides preliminary information on development of the FFF process using different powder types to demonstrate sensitivity and the characterization of these sample components. This full solid-state manufacturing feasibility study will be completed and reported in a final evaluation during 2024.

The study included investigation used two 14YWT ODS powder batches that provided information on the effect of different powder morphologies on manufacturability with FFF. The two 316SS powders demonstrated the effect of powder size on manufacturability. Two product forms, namely a honeycomb structure and flat samples, were manufactured to demonstrate the flexibility of product form.

Both ODS steel and 316H custom filaments were successfully fabricated with a powder loading of 65% and 62% respectively. Specific filament fabrication and printing parameters for each material type and powder were determined to achieve the successful printing, and therefore show feasibility to use FFF for component manufacturing. However, process optimization for more dense parts is necessary and the scalability needs further work.

The research results provided in this report provide evidence that it is feasible to print ODS steel as well as 316H SS using the FFF solid-state fabrication process with the following conclusions:

- The filament fabrication process and printing are sensitive for the powder morphology, size, and size distribution mainly due to the flowability of the filament extrusion and the sinter effectiveness.
- Custom powder can be used for FFF; therefore, an in-house PNNL capability was developed enabling ODS and 316H SS powder loading techniques.
- Although effective printing and subsequent sintering did occur, further optimization is needed to fully fabricate structural sound components.

5.0 References

[1] Li, M., Andersson D., Dehoff R., Jokisaari A., van Rooyen, I., Cairns-Gallimore, D., Advanced Materials and Manufacturing Technologies (AMMT) 2022 Roadmap , ANL-23-12, September 2022.

[2] Tuncer, N., Bose, A., Solid State Manufacturing: A Review, JOM, Vol. 72, No. 9, 2020.

[3] Azushima, A., Kopp, R., Korhonen, A., et al., Severe plastic deformation (SPD) processes for metals, CIRP Annals 57(2) (2008) 716-735.

[4] Ohnuma, M., Suzuki, J., Ohtsuka, S., Kim, S. W., Kaito, T., Inoue, M., & Kitazawa, H. (2009). A new method for the quantitative analysis of the scale and composition of nanosized oxide in 9Cr-ODS steel. Acta materialia, 57(18), 5571-5581.

[5] Ukai, S., & Fujiwara, M. (2002). Perspective of ODS alloys application in nuclear environments. Journal of Nuclear Materials, 307, 749-757.

[6] Autones, L., Aubry, P., Ribis, J., Leguy, H., Legris, A., & de Carlan, Y. (2023). Assessment of Ferritic ODS Steels Obtained by Laser Additive Manufacturing. Materials, 16(6), 2397.

Appendix A – SEM and Microscope Images of Sintered Parts

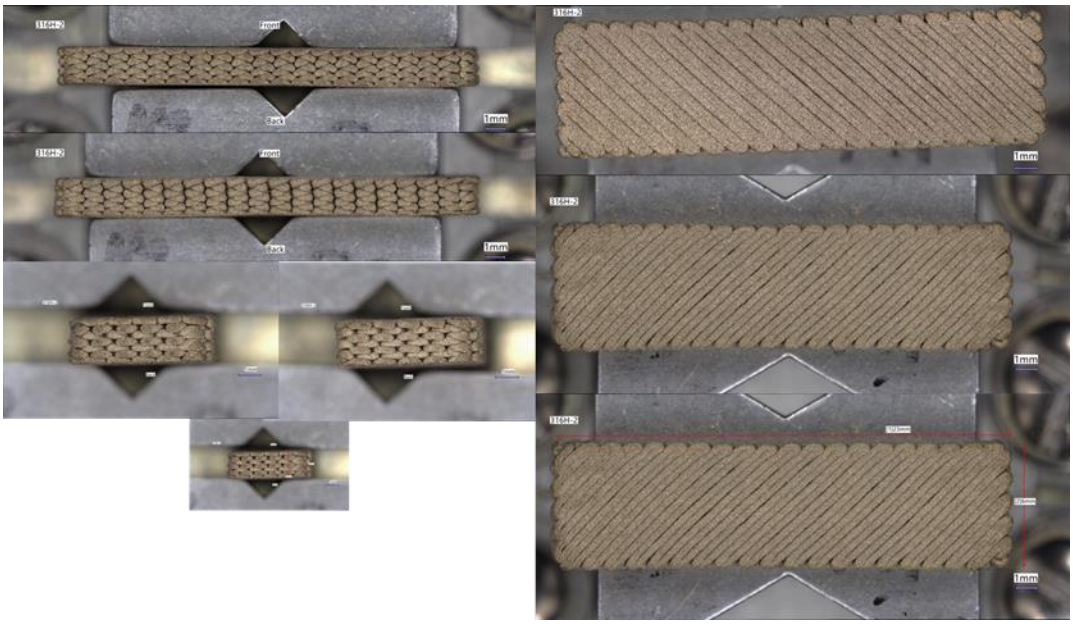

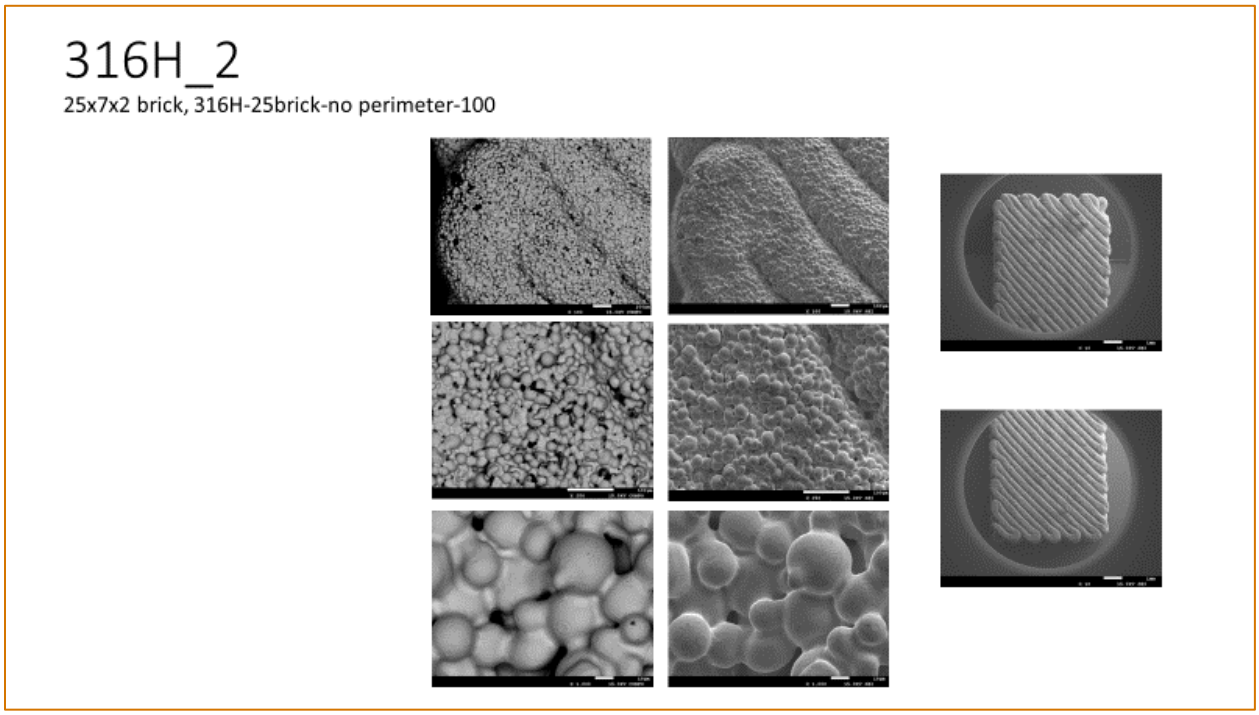

Figure 43. 316H Print#2, No Perimeter-100% Filled- Optical and SEM Images

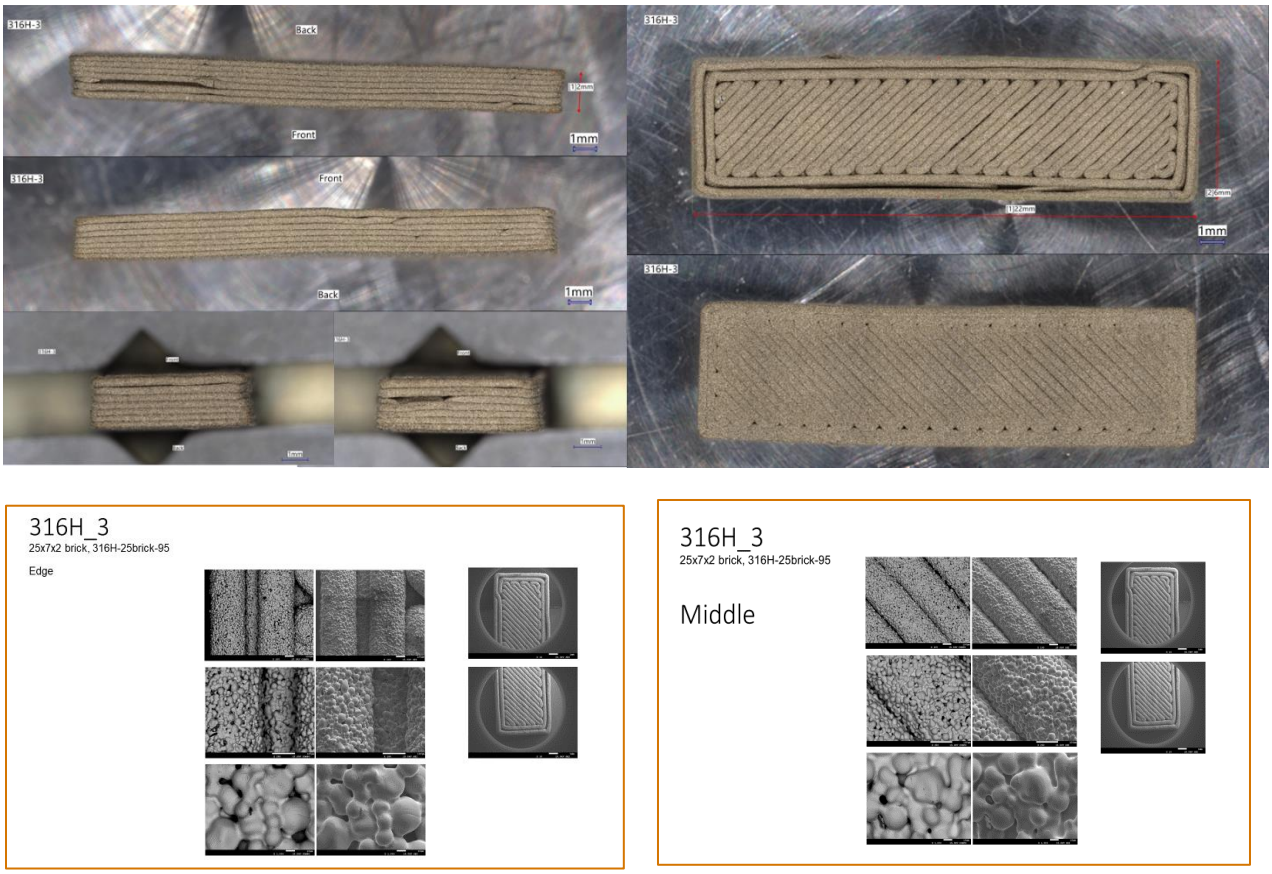

Figure 44. 316H Print#3, With Perimeter-95% Filled- Optical and SEM Images.

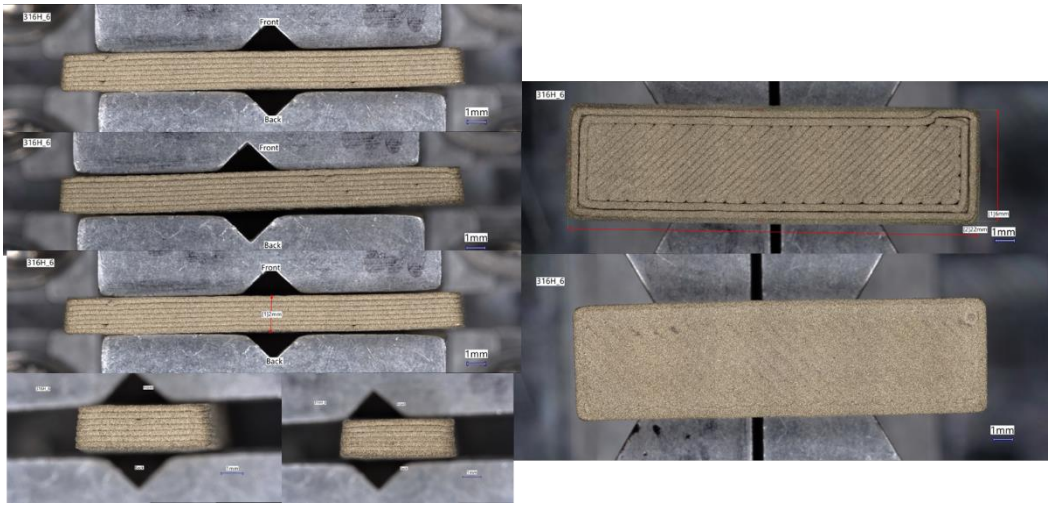

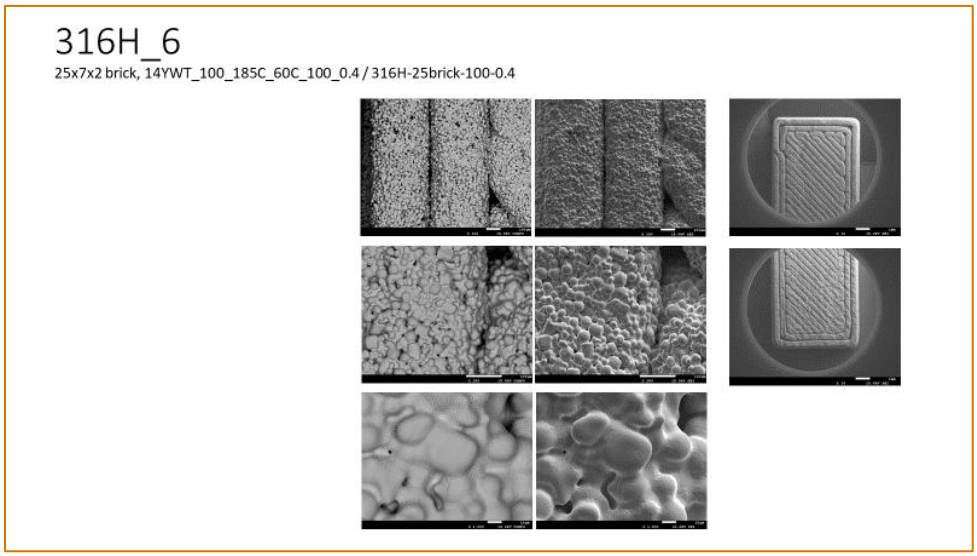

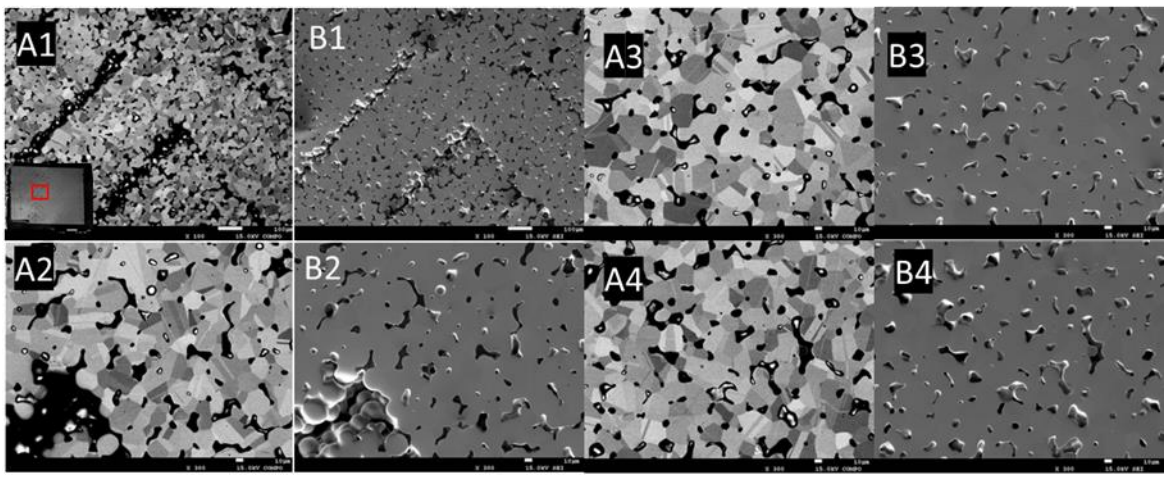

Figure 45. 316H Print#6, With Perimeter-100% Filled- Optical and SEM Images, bottom A1-A4 SEM backscatter and B1-B4 secondary imaging mode.

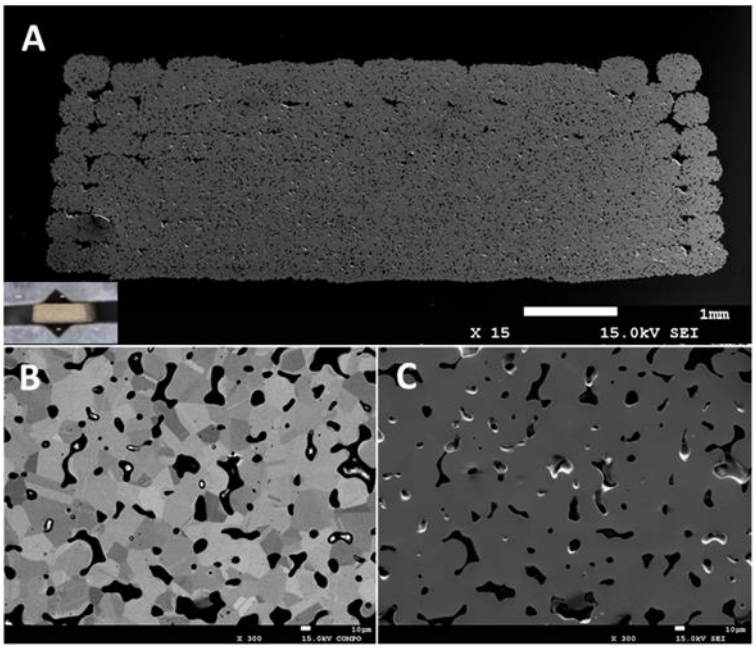

Figure 46. 316H Print#6, With Perimeter-100% Filled- Optical and SEM Images Cross sectional view (insert) (A). High magnification micrographs exhibit image contrast (B) showing distribution of grains. Pore density and geometries is observed within the materials (C).

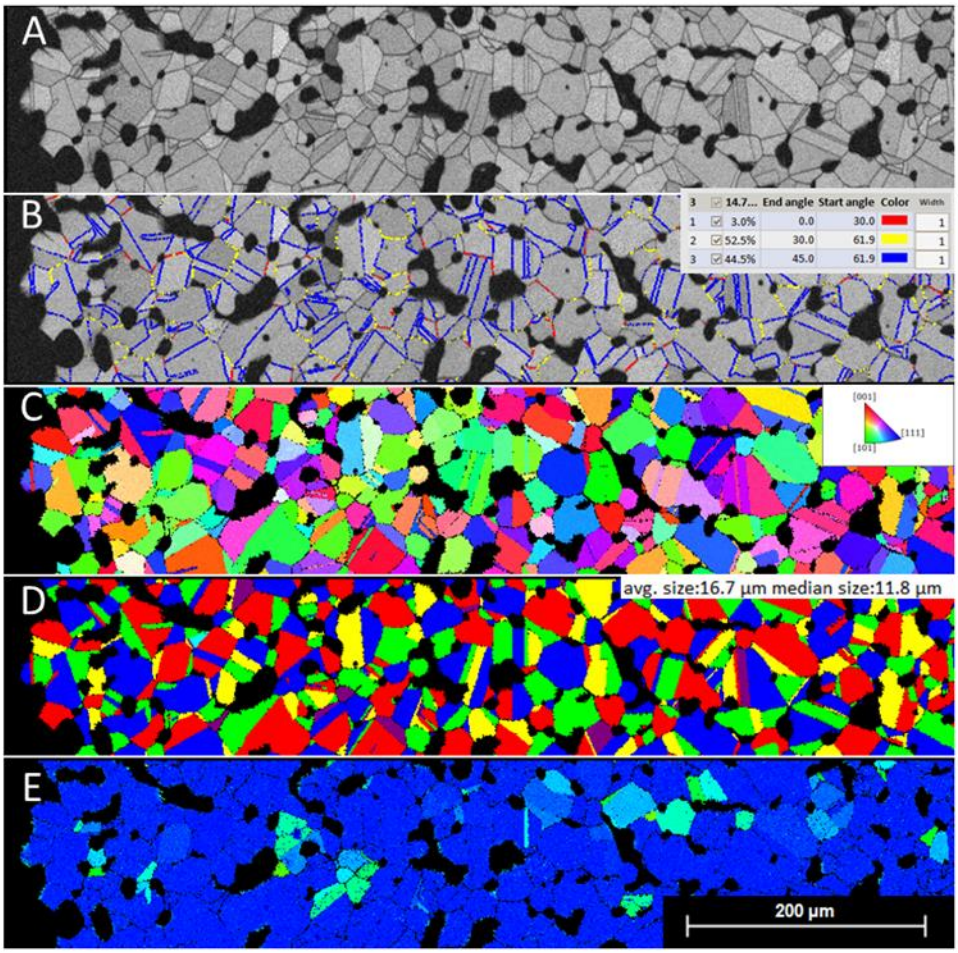

Figure 47. 316H Print#6, Electron backscatter diffraction (EBSD) of the planar prepared print 6 at the edge.

(A) The Pattern Quality Map offers a grayscale representation of Kikuchi pattern quality. (B) The Grain Boundary Distribution visually demonstrates the distribution and density of grain boundaries, differentiated by color for different angles (insert). (C) The Grain Orientation Map displays crystallographic orientations with varying colors to aid in grain orientation identification (insert). (D) The Grain Distribution map reveals grain size and spatial arrangement (insert). (E) The MO Average measures misalignment at grain boundaries, providing valuable information about structural integrity (strain) and processing effects.

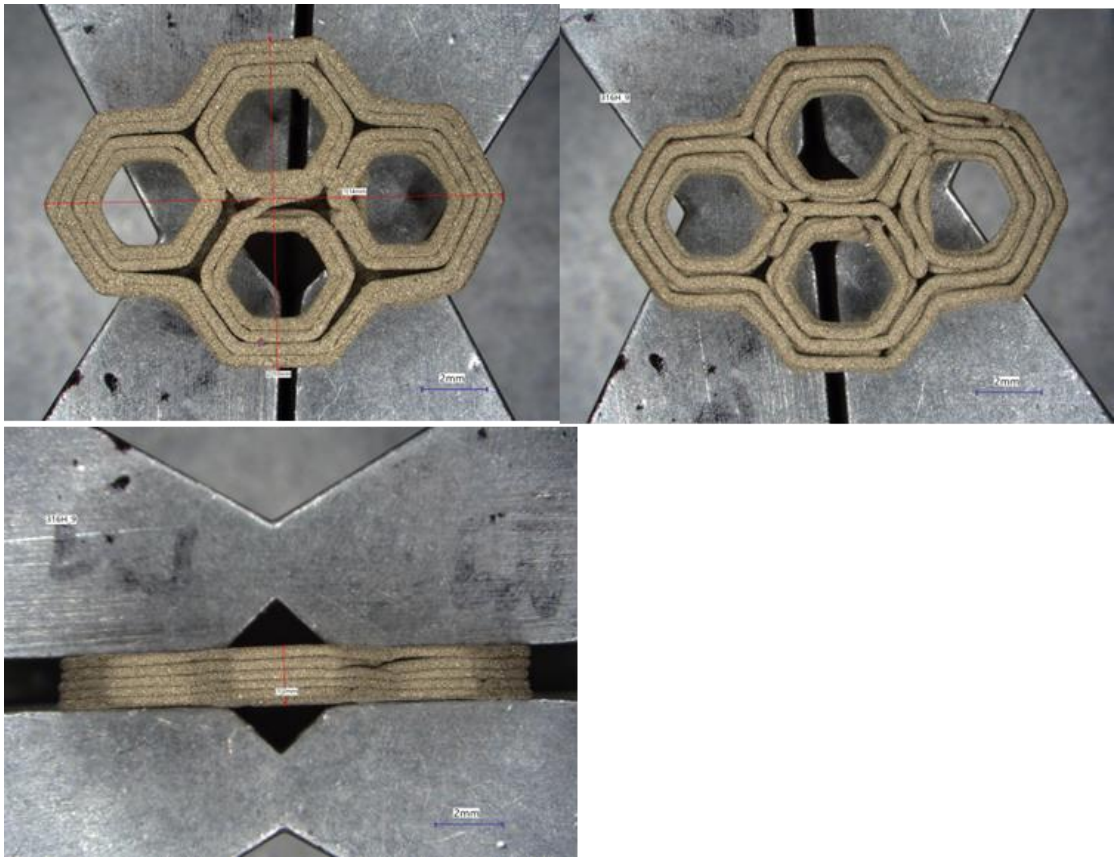

Figure 48. 316H Print#9, With Perimeter-100% Filled- Optical Images

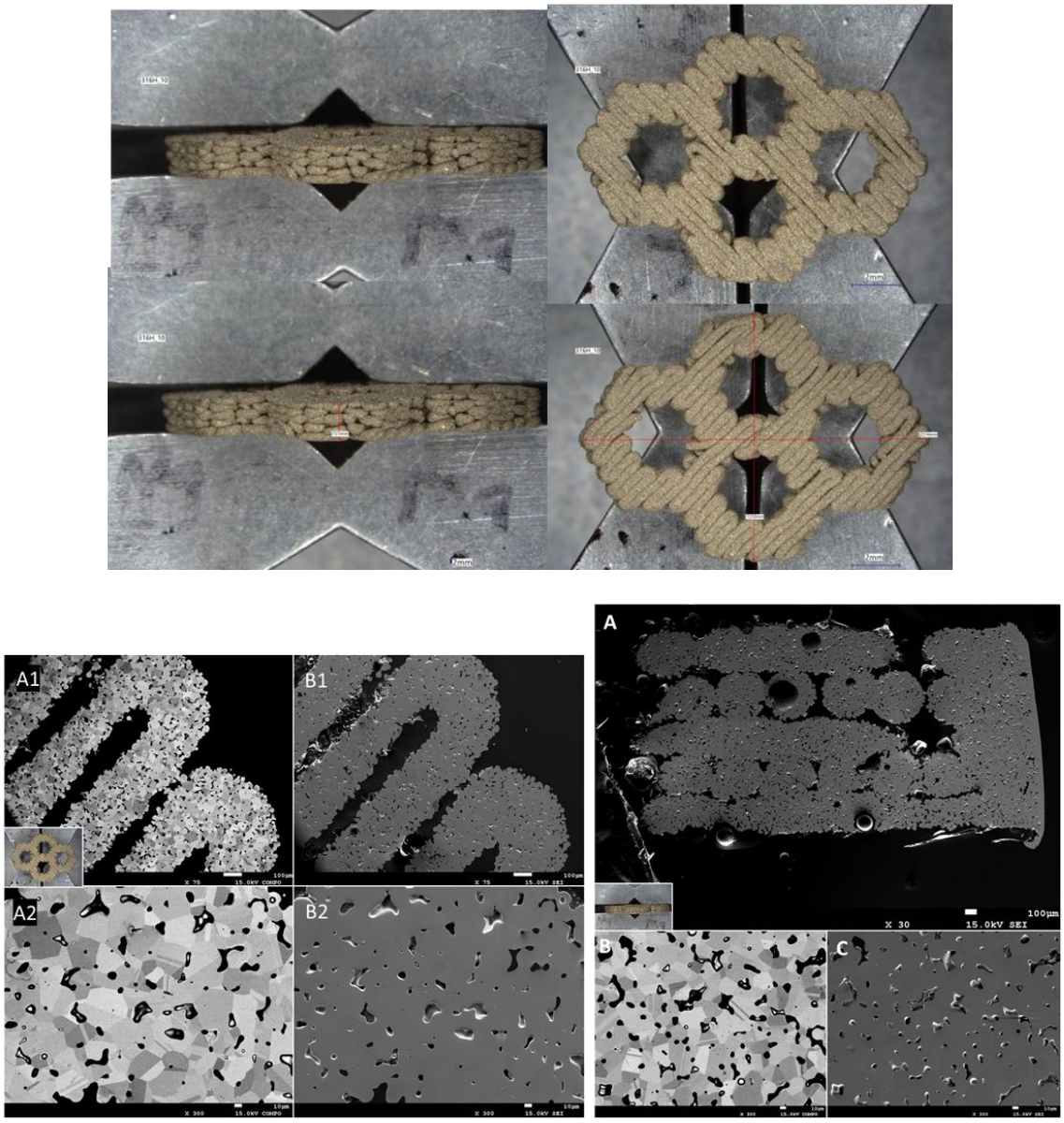

Figure 49. 316H Print#10 Without Perimeter-100% Filled Optical Images Top. SEM Cross sectional view, A (RHS). SEM backscatter A1, A2 and B and secondary imaging mode B1, B2 and C.

Pacific Northwest National Laboratory

902 Battelle Boulevard
P.O. Box 999
Richland, WA 99354

1-888-375-PNNL (7665)

www.pnnl.gov